Economic Geology, v. 114, no. 7, pp. 1389–1414

Origin of Au-Rich Carbonate-Hosted Replacement Deposits of the Kassandra Mining District, Northern Greece: Evidence for Late Oligocene, Structurally Controlled, and Zoned Hydrothermal Systems

Chris R. Siron,[1,†] John F.H. Thompson,[1] Tim Baker,[2] Robert Darling,[3] and Gregory Dipple[4]

[1]*Department of Earth and Atmospheric Sciences, Cornell University, Ithaca, New York 14853, USA*

[2]*Eldorado Gold Corporation, Vancouver, British Columbia V6C 2B5, Canada*

[3]*Geology Department, State University of New York, Cortland, New York 13045, USA*

[4]*Mineral Deposit Research Unit, University of British Columbia, Vancouver, British Columbia V6T 1Z4, Canada*

Abstract

The Au-rich polymetallic massive sulfide orebodies of the Kassandra mining district belong to the intrusion-related carbonate-hosted replacement deposit class. Marble lenses contained within the Stratoni fault zone host the Madem Lakkos and Mavres Petres deposits at the eastern end of the fault system, where paragenetically early skarn and massive sulfide are spatially associated with late Oligocene aplitic and porphyritic dikes. Skarn transitions into predominant massive and banded replacement sulfide bodies, which are overprinted by a younger assemblage of boulangerite-bearing, quartz-rich sulfide and late quartz-rhodochrosite vein breccias. The latter style of mineralization is most abundant at the Piavitsa prospect at the western end of the exposed fault system. The sulfide orebodies at the Olympias deposit are hosted by marble in association with the Kassandra fault, where textural and mineralogical similarities to the sulfide bodies within the Stratoni fault zone suggest a genetic relationship. Estimated trapping temperatures and pressures based on fluid inclusion data indicate that carbonate replacement mineralization took place at depths less than about 5.9 km.

Carbon and oxygen isotope patterns in carbonate from the Stratoni fault zone support isotopic exchange principally through fluid–wall-rock interaction, whereas decarbonation and fluid-rock exchange reactions were important at the Olympias deposit. Carbonate minerals associated with skarn and replacement sulfide throughout the district have isotopic compositions that are consistent with formation from a hydrothermal fluid of magmatic origin. Lower homogenization temperatures and salinities in the younger quartz-rich sulfide assemblage and quartz-rhodochrosite vein breccias, together with low $\delta^{18}O$ values of gangue carbonate, suggest dilution of a primary magmatic fluid with meteoric water late in the evolution of the hydrothermal system in both the Olympias area and the Stratoni fault zone. The replacement sulfide orebodies in the district likely inherited their uniform Pb isotope composition from a late Oligocene igneous source and the isotopically heterogeneous metamorphic basement units.

Metal distribution patterns at the scale of the Stratoni fault zone show diminishing Cu concentration with decreasing Pb/Zn and Ag/Au ratios from Madem Lakkos to Mavres Petres and the Piavitsa prospect in the west. The sulfide orebodies at the Olympias deposit exhibit elevated Cu values in the east with increasing Pb/Zn and Ag/Au ratios down-plunge to the south-southwest. Metal concentration and ratios support zoning related to temperature and solubility changes with increasing distance from a probable magmatic source. Structural and igneous relationships, together with fluid inclusion microthermometric and carbon-oxygen isotope data and metal distribution patterns, are supportive of a zoned hydrothermal system that exceeded 12 km along the Stratoni fault zone, sourced by an igneous intrusion to the southeast of the Madem Lakkos deposit. The Olympias replacement sulfide orebodies, associated with the Kassandra fault, resulted from a local hydrothermal system that was likely derived from a concealed igneous intrusion to the east of the deposit.

Introduction

The Serbo-Macedonian metallogenic province (Janković, 1997; Serafimovski, 2000) of the greater Tethyan mineral belt forms an NW-trending zone of Oligo-Miocene porphyry Au-Cu, Cu skarn, and Au-rich polymetallic vein and carbonate-hosted replacement deposits that extends from Serbia and Kosovo through the Republic of Macedonia and into the Kassandra mining district on the eastern Chalkidiki peninsula of northern Greece (Fig. 1). Past mining of the Madem Lakkos deposit produced approximately 13.5 million tonnes (Mt) of Ag-Pb-Zn ore (Forward et al., 2010). The actively producing Mavres Petres and Olympias mines contain measured and indicated resources of 0.55 Mt at 212 g/t Ag, 8.1% Pb, and 11.0% Zn, and 15.1 Mt at 8.97 g/t Au, 146 g/t Ag, 4.9% Pb, and 6.5% Zn, respectively (Eldorado Gold Corporation, 2017a). The Piavitsa prospect contains an inferred resource of 10.5 Mt grading 5.7 g/t Au (Eldorado Gold Corporation, 2017a). At the present time, approximately 10 Moz Au is contained within these sulfide orebodies, including the Skouries porphyry Au-Cu deposit, making the Kassandra mining district one of the most economically significant mining camps in southeast Europe.

Carbonate replacement sulfide ore deposits in the Kassandra mining district occur within the Rhodope metamorphic province, a complex amphibolite-facies metamorphic rock assemblage in the hinterland of the Hellenic orogen (Burg, 2012). In the study area, crystalline metamorphic basement rocks largely belong to the Permo-Carboniferous Rhodope

†Corresponding author: e-mail, crsiron@gmail.com

ISSN 0361-0128; doi:10.5382/econgeo.4664; 26 p.
Digital appendices are available in the online Supplements section.

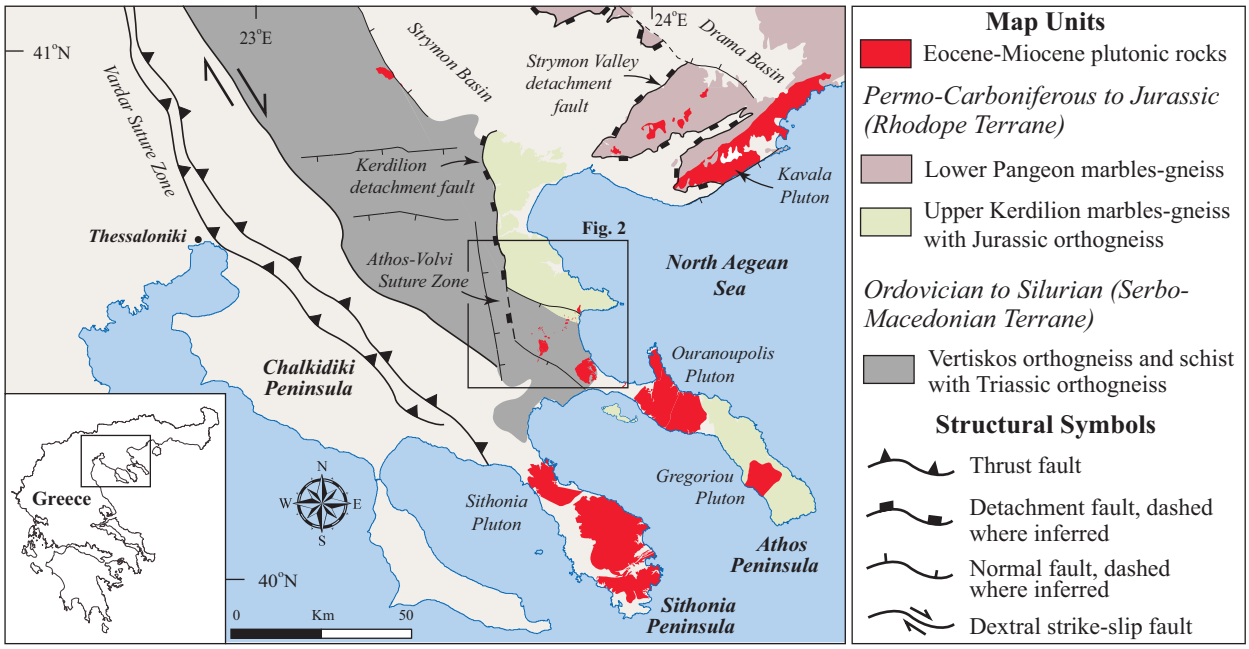

Fig. 1. Simplified regional geologic map of northeastern Greece, modified after Kydonakis et al. (2014), showing the major tectonic units described in the text. The Strymon Valley and Kerdilion detachment faults were adapted from Dinter (1998) and Brun and Sokoutis (2007), respectively. The location of the Athos-Volvi suture zone is after Himmerkus et al. (2005).

Kerdilion unit and the Ordovician-Silurian Serbo-Macedonian Vertiskos unit (Fig. 1; Kockel et al., 1977). The polymetallic sulfide orebodies at the Olympias, Madem Lakkos, and Mavres Petres deposits (Fig. 2) are hosted by Kerdilion marbles that lie in contact with preexisting ductile structures, but mineralization was coeval with extensional deformation and semibrittle to brittle faults that were active during the late Oligocene (Fig. 2; Siron et al., 2018).

A prominent NE-trending belt of postcollisional intrusive rocks crops out within the Kassandra mining district (Fig. 2). This belt is defined by two major magmatic episodes in the late Oligocene to early Miocene, which are linked to two distinct metallogenic events (Frei, 1992, 1995; Gilg, 1993; Gilg and Frei, 1994; Hahn et al., 2012; Hahn, 2014; Siron et al., 2016, 2018). Late Oligocene high-K calc-alkaline magmas are closely associated with the carbonate replacement massive sulfide orebodies, whereas porphyry Au-Cu mineralization resulted from early Miocene shoshonitic magmatism in the Skouries area (Fig. 2; Siron et al., 2016). The late Oligocene Stratoni granodiorite stock and spatially related granitic aplite dikes and sills occurring within the Stratoni fault zone were originally interpreted as the magmatic source responsible for the sulfide orebodies in the Madem Lakkos area (Neubauer, 1957; Nicolaou, 1960, 1964). This interpretation has been refuted by other studies, which tentatively propose that the porphyritic granodiorite stocks and dikes in the Fisoka area represent the source of fluids for the replacement sulfide ore deposits (Frei, 1992; Gilg, 1993). Nebel et al. (1991) similarly proposed that either the Fisoka or Stratoni stocks could have contributed to skarn mineralization in the Madem Lakkos area. Sulfide orebodies at the Olympias deposit in the north were considered by Kalogeropoulos et al. (1989) and Hahn (2014) as the distal expressions of the hydrothermal system that resulted in the sulfide orebodies at Madem Lakkos. A syngenetic origin to the massive sulfide at Madem Lakkos and Olympias has been largely discredited based on structural relationships and geochronological evidence (e.g., Gilg and Frei, 1994; Haines, 1998; Hahn, 2014; Siron et al., 2016, 2018). Regardless, the causative magmatic source for the hydrothermal system(s) resulting in the sulfide orebodies within the Stratoni fault zone and at the Olympias deposit remains uncertain.

This study utilizes a variety of techniques and data sources to constrain the origin of the carbonate replacement mineralization in the Kassandra mining district. Detailed petrography on representative ore styles and a comprehensive drill core geochemical database assisted in discerning the metal deportment and zonation patterns at the district and deposit scale, with fluid inclusion microthermometry of primary, synmineral quartz gangue used to investigate the temperatures of ore formation. Carbon and oxygen isotopes of marble and carbonate gangue minerals associated with the sulfide bodies were evaluated to identify possible fluid sources and to model the physiochemical processes responsible for replacement sulfide and vein-breccia styles of mineralization in the district. Lead isotope data from the sulfide ore and igneous K-feldspar phenocrysts from selected late Oligocene and early Miocene intrusions were also obtained to investigate the relationships between intrusions and the sulfide deposits. These results, combined with previously published fluid inclusion and isotopic data (e.g., Gilg, 1993), are presented here to provide constraints on the origin and source of the hydrothermal fluid(s) responsible for the carbonate replacement deposits in the Kassandra mining district.

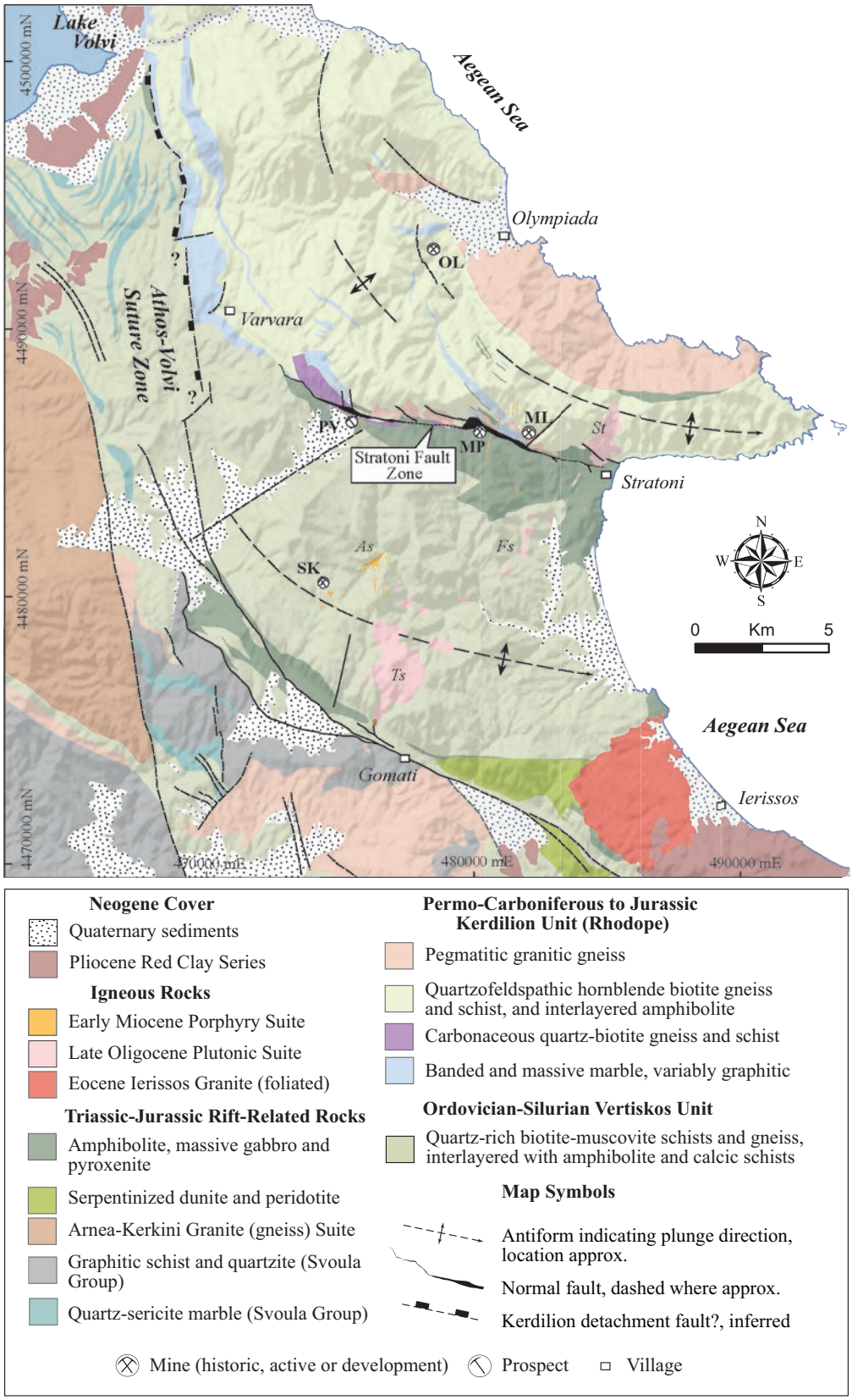

Fig. 2. Geologic map of the Kassandra mining district, modified after Kockel et al. (1977) and Siron et al. (2018). Coordinates are displayed in the Greek Geodetic Coordinate System (GGRS 87 Greek Grid). Abbreviations are as follows: As = Aspro Lakkos porphyry stock, Fs = Fisoka stock, ML = Madem Lakkos deposit, MP = Mavres Petres deposit, OL = Olympias deposit, PV = Piavitsa prospect, SK = Skouries deposit, St = Stratoni stock, Ts = Tsikara composite stock.

Carbonate Replacement Deposits

The polymetallic (Au-Ag-Pb-Zn-Cu) carbonate-hosted sulfide orebodies within the Kassandra mining district include the past-producing Madem Lakkos deposit and the actively producing Mavres Petres and Olympias deposits. These orebodies have attracted research for over 90 years (e.g., Sagui, 1928) with a wealth of mineralogical, isotopic, and fluid inclusion studies focused on the Madem Lakkos and Olympias deposits (Nicolaou, 1960, 1964; Nicolaou and Kokonis, 1980; Kalogeropoulos and Economou, 1987; Kalogeropoulos et al., 1989; Kilias and Kalogeropoulos, 1989; Mantzos, 1989; Nebel, 1989; Nebel et al., 1991; Gilg, 1993; Gilg and Frei, 1994; Kilias and Madsen, 1994; Kilias et al., 1996; Haines, 1998; Hahn et al., 2012; Hahn, 2014), as well as a number of unpublished consulting reports. In this section, we summarize previous mineralogical work aided by petrological observations from polished sections of representative sulfide ore styles from the Olympias, Mavres Petres, and Piavitsa areas.

Olympias deposit

The Olympias deposit is located 6 km north of the Stratoni fault zone (Fig. 2). Replacement-style sulfide orebodies are hosted by graphitic marble interlayered within a sequence of quartzofeldspathic biotite gneiss, amphibolite, and plagioclase-microcline orthogneiss (Kalogeropoulos et al., 1989; Siron et al., 2016). The massive sulfide orebody plunges shallowly to the southeast, subparallel to the orientation of F2 fold hinges and a locally developed L2 intersection lineation. The locations of the sulfide lenses, however, are largely controlled by strands of the ductile-brittle Kassandra fault and subhorizontal ductile shear zones that occur in the intervening area. Crosscutting structural relationships and $^{40}Ar/^{39}Ar$ geochronology (22.6 ± 0.3 Ma) indicate that carbonate replacement mineralization occurred by the latest Oligocene, coincident with the early stage of postdeformation magmatism in the region (Siron et al., 2018).

Sulfide mineralogy of the Olympias deposit consists of coarse-grained, massive and banded lenses of sphalerite-galena-pyrite that transition into pyrite-rich intervals and arsenopyrite. Sphalerite-rich sulfide zones commonly display rod-like pyrite textures (Fig. 3A, B), which may represent the pseudomorphic replacement of marcasite as documented at the Leadville deposit in Colorado (Thompson and Arehart, 1990). This distinct ore texture is also recognized at the Mavres Petres deposit and indicates a similar paragenetic relationship. Chalcopyrite is a common minor sulfide mineral, and it typically occurs as inclusions in sphalerite, along sphalerite grain boundaries, or occupying microfractures (Kalogeropoulos and Economou, 1987). Accessory minerals including graphite, pyrrhotite, marcasite, and stibnite occur in trace quantities (Fig. 3C), with mackinawite, enargite, geocronite, cubanite, bornite, and covellite also reported in previous studies (Nicolaou and Kokonis, 1980; Kalogeropoulos et al., 1989). Unpublished metallurgical studies and consulting reports identified Ag-bearing tetrahedrite (freibergite) and bournonite as intergrowths and inclusions in galena as well as fracture fill in sphalerite. In rare cases, gold has been identified as inclusions in arsenopyrite (Ross and Rhys, 2013). Secondary ion mass spectroscopy results in an unpublished company report indicate that Ag and Au primarily occur in solid solution with galena and arsenopyrite (including arsenical pyrite), respectively.

A paragenetically younger quartz-rich sulfide assemblage locally overprints the early replacement massive sulfide ore horizons. These quartz-rich sulfide bodies consist of interlocking, euhedral and growth-zoned quartz accompanied by interstitial fibrous boulangerite and arsenopyrite with subordinate pyrite, galena, and sphalerite containing minor inclusions of chalcopyrite (Fig. 3D, E). Boulangerite commonly replaced pyrite and sphalerite (Fig. 3F). Mineralized silicified breccias also occur within the Olympias deposit and consist of matrix-supported, chaotically arranged subangular to angular clasts of sericite-altered granite gneiss, marble, and sulfide (Siron et al., 2018). The breccia matrix consists of dark gray chalcedonic quartz containing disseminated, euhedral pyrite and bladed arsenopyrite. These quartz-rich replacement zones and mineralized silicified breccias are commonly associated with quartz-rhodochrosite alteration of the surrounding wall rock and are most commonly developed in the northern and eastern portions of the Olympias deposit.

Fig. 3. Thin section billets (~3 cm in length) and corresponding reflected light photomicrographs of representative sulfide samples from the carbonate replacement sulfide deposits of the Kassandra mining district: (A-C) sphalerite-rich massive sulfide with distinctive radiating rod-textured pyrite from the Olympias deposit; (B) tarnished pyrite rods penetrating and replacing sphalerite; (C) inclusions of relic graphite and blebs of chalcopyrite within sphalerite; (D, E) example of quartz-rich sulfide from the Olympias deposit showing prismatic clear quartz and sulfide-bearing blue quartz intergrown with pyrite, minor sphalerite, and fine-grained boulangerite; (E) example of cubic pyrite crystal partially replaced by younger anhedral sphalerite; (F) boulangerite (silver color) occurring within voids between quartz grains and invading fractures within sphalerite. Note the abundant chalcopyrite inclusions in sphalerite. (G-I) Arsenopyrite-rich pyrite-sphalerite > galena massive sulfide from the Mavres Petres deposit; (H) arsenopyrite containing inclusions of pyrite and sphalerite and showing a typical brecciated texture caused by syn- to late-mineral calcite; (I) partial cross-polarized reflected light image of galena in part replaced by boulangerite with quartz forming the matrix to brecciated pyrite; (J-L) typical quartz-rich disseminated sulfide from the Mavres Petres deposit showing patchy pyrite and fine-grained boulangerite imparting the bluish-gray hue to the quartz; (K) common occurrence of boulangerite occupying void space between quartz grains; (L) interwoven mesh of boulangerite and quartz with euhedral oscillatory-zoned quartz crystals; (M-O) base metal-rich quartz-carbonate vein; (N) sphalerite overgrown by euhedral arsenopyrite, quartz, and carbonate gangue; (O) euhedral pyrite crystals showing arsenopyrite overgrowths on margin of quartz vein; (P-R) typical quartz-rhodochrosite vein displaying vibrant pink color and exhibiting domains of clear crustiform quartz and dark chalcedonic quartz hosting fine-grain boulangerite and sphalerite; (Q) boulangerite occurring within chalcedonic quartz at margin of rhodochrosite; (R) sphalerite showing partial replacement by boulangerite within chalcedonic quartz vein. Abbreviations: Asp = arsenopyrite, Boul = boulangerite, Cal = calcite, Cp = chalcopyrite, Ga = galena, Gr = graphite, Ms = muscovite, Py = pyrite, Qtz = quartz, Rds = rhodochrosite, RL = reflected light, Sp = sphalerite.

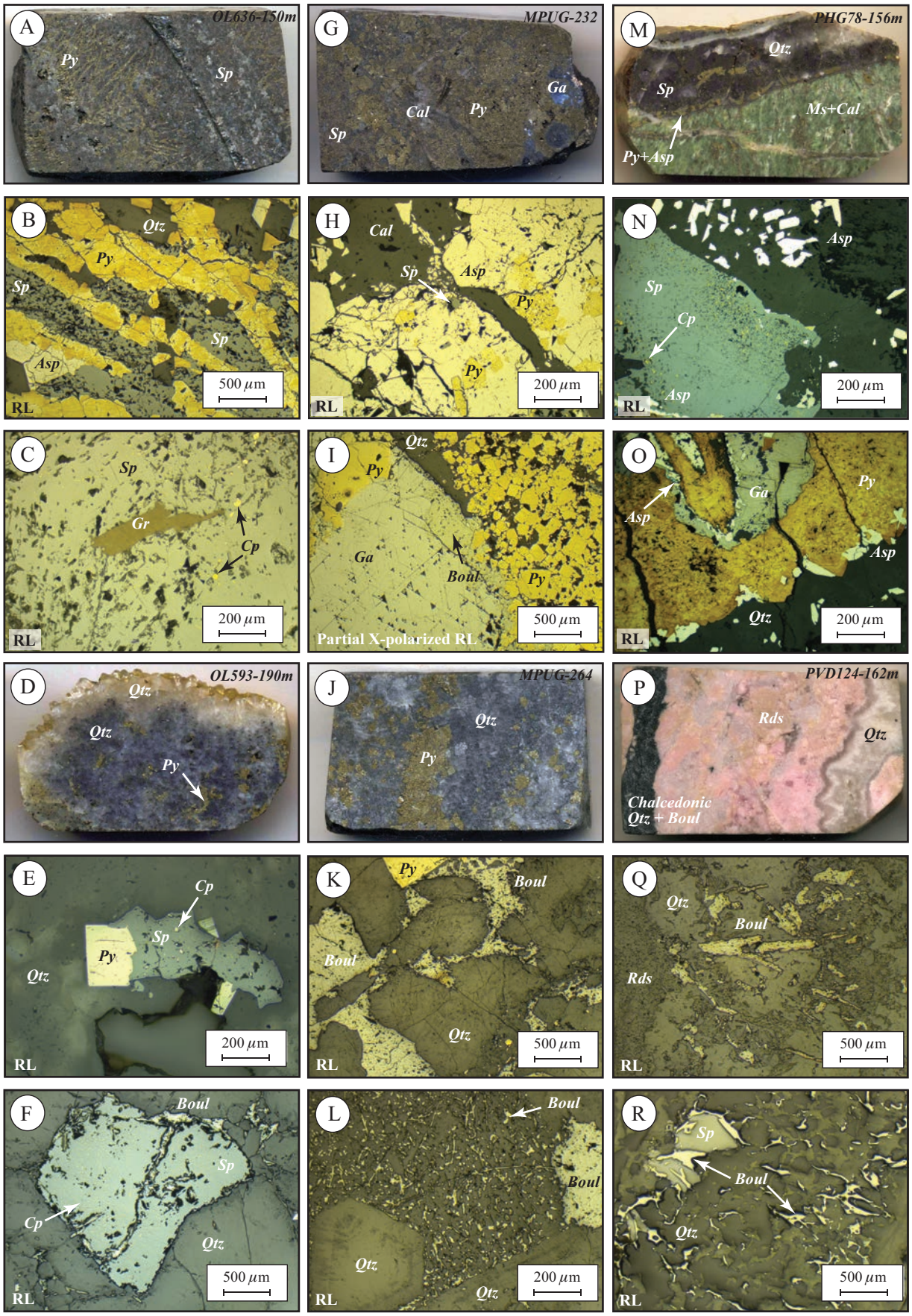

Deposits of the Stratoni fault zone

The Stratoni fault zone is a complexly mineralized structural corridor that hosts the Madem Lakkos and Mavres Petres deposits and the Piavitsa prospect (Fig. 2). Skarn and replacement-style orebodies at the Madem Lakkos deposit occur at the eastern end of the Stratoni fault zone and within 2 km of the Stratoni and the Fisoka granodiorite stocks to the east and south-southeast, respectively (Fig. 2). Previous studies have described a spatial and temporal relationship between aplitic and porphyritic dikes of late Oligocene age and sulfide mineralization (Gilg and Frei, 1994). Massive sulfide in the Madem Lakkos area is hosted by marble lenses that are localized along faults and within F2 fold hinges associated with a major antiform in the footwall of the Stratoni fault zone (Nebel, 1989; Nebel et al., 1991; Gilg, 1993; Gilg and Frei, 1994; Haines, 1998; Siron et al., 2016, 2018). To the west of Madem Lakkos, sulfide orebodies at the Mavres Petres deposit are similarly hosted by marbles contained within a strongly carbonaceous segment of the Stratoni fault zone (Siron et al., 2018), with discontinuous sulfide lenses and quartz-Mn–rich replacement bodies occurring farther to the west (Fig. 2). Crustiform-textured, Au-bearing quartz-rhodochrosite ± rhodonite vein breccias persist throughout the district but are largely concentrated at the Piavitsa prospect. The vein-breccia system in the Piavitsa area is principally restricted to the hanging wall of the Stratoni fault zone and localized along N-S–striking faults (Siron et al., 2018).

Madem Lakkos deposit: The replacement orebodies at the Madem Lakkos deposit are principally restricted to marble lenses contained within and adjacent to the Stratoni fault zone. Ore consists of skarn and massive sulfide with a younger and volumetrically larger sulfide assemblage termed "disseminated sulfide" by Nebel (1989) and Gilg (1993). The sulfide mineralogy of the Madem Lakkos deposit described here is adapted from previous work (Nicolaou, 1964; Nebel, 1989; Nebel et al., 1991; Gilg, 1993; Haines, 1998). An early skarn mineralizing event is evident at the deposit and consists of a high-temperature mineral assemblage of andradite garnet-diopside ± anhydrite with epidote and magnetite. Retrograde alteration of primary calcic skarn minerals to hydrous phases (e.g., Fe-bearing chlorite and actinolite) is accompanied by pyrite and chalcopyrite with minor pyrrhotite, mackinawite, bismuthinite, cubanite, scheelite, and trace amounts of galena, tennantite, galenobismuthinite, aikinite, and cosalite. Magnesian skarns are spatially associated with dolomitic marble and consist of a prograde mineral assemblage of forsteritic olivine, magnetite, and pyrite. Retrograde alteration of primary skarn minerals resulted in the conversion of olivine to serpentine and talc and the development of other hydrous mineral phases including tremolite, phlogopite, Mg chlorite, and the addition of calcite and anhydrite. Pyrite associated with retrograde alteration contains inclusions of pyrrhotite, mackinawite, cubanite, and chalcopyrite.

The mineralogy of the skarn-free massive sulfide bodies includes galena, sphalerite, and pyrite with minor to trace amounts of chalcopyrite, arsenopyrite, and tetrahedrite-tennantite. Pyrrhotite occurs in abundance in association with pyrite-rich replacement bodies (Nicolaou, 1964). The younger disseminated sulfide phase partially overprints the massive sulfide and is characterized by replacement and breccia textures, veinlets, and open-space cavity fill. This phase of mineralization is quartz rich and consists of pyrite with lesser sphalerite, galena, arsenopyrite, and chalcopyrite, minor tetrahedrite-tennantite and boulangerite, and trace amounts of other sulfosalt minerals. Quartz and rhodochrosite typically occur with the massive and disseminated sulfide phases and are the principal gangue minerals in the late-mineral vein breccias (Siron et al., 2016, 2018).

Mavres Petres deposit: The replacement sulfide orebody at the Mavres Petres deposit exhibits mineral textures and a paragenesis that are broadly similar to the sulfide bodies at the Madem Lakkos and Olympias deposits. Replacement-style sulfide consists of pyrite, sphalerite, and galena in varying proportions with accessory arsenopyrite, stibnite, and minor boulangerite and chalcopyrite (Fig. 3G-I; Siron et al., 2016). Massive arsenopyrite occurs locally and is generally late in the sulfide paragenesis, infilling fractures and replacing previously deposited sulfide minerals. Replacement sulfide bodies are overprinted by a quartz-rich sulfide assemblage, characterized by replacement and breccia styles of mineralization with open-space and vuggy textures. The quartz-rich sulfide style of mineralization at the Mavres Petres deposit is considered equivalent to the disseminated sulfide phase described at the Madem Lakkos deposit (e.g., Gilg, 1993) based on mineralogical similarities and fluid inclusion evidence presented later. Sulfide minerals associated with quartz-rich mineralization consist of pyrite and sphalerite containing chalcopyrite inclusions (Fig. 3J). Boulangerite is characteristically associated with this event and occurs as fibrous crystals that commonly form masses and anhedral mosaics interstitial to prismatic and zoned quartz (Fig. 3K, L). Crustiform-textured quartz-rhodochrosite ± rhodonite veins and breccias, similar to those at the Piavitsa prospect discussed below, are incipiently developed in the western portions of the Mavres Petres deposit and are recognized as the youngest phase of mineralization based on crosscutting relationships (Siron et al., 2018). Quartz-rhodochrosite vein breccias display a mineralogy similar to that of the quartz-rich sulfide assemblage but predominantly contain boulangerite ± arsenopyrite.

Piavitsa prospect: Replacement-style sulfide bodies in the Piavitsa area occur as discontinuous lenses, which are typically brecciated and hosted by marble and graphite-bearing carbonaceous quartz-biotite gneiss and schist within the Stratoni fault zone (Siron et al., 2018). The sulfide bodies exhibit a mineralogy similar to that of the replacement ore at the Mavres Petres deposit. Drill core intercepts show that marble lenses are variably replaced by quartz-rhodochrosite intergrown with dolomite, pale green mica, and patchy replacement sulfide intervals consisting of pyrite, galena, sphalerite, and arsenopyrite (Fig. 3M-O; Siron et al., 2016). A younger and overprinting style of mineralization consisting of quartz-rhodochrosite ± rhodonite veins and breccias exhibits a diagnostic pink coloration and crustiform textures with open-space, clear to milky prismatic quartz and black chalcedonic quartz domains (Fig. 3P). Fine-grained pyrite and arsenopyrite are associated with rhodochrosite and prismatic quartz. Fibrous boulangerite crystals, characteristic of this event, typically occupy black chalcedonic quartz domains (Fig. 3Q). Sphalerite is a minor mineral associated with the black chalcedonic

quartz and is commonly replaced by boulangerite (Fig. 3R). Chalcopyrite is a rare sulfide mineral phase and is generally late in the mineral paragenesis.

Metal Zonation

Carbonate-hosted replacement deposits commonly show metal zonation patterns where Cu-(Au-W-Mo) is elevated proximal to mineral-related igneous intrusions with increasing Ag-Mn concentrations in the distal parts of the hydrothermal system (Megaw, 1998). This study utilized a multielement geochemical database to identify the distribution of metals in and around the orebodies within the Stratoni fault zone and at the Olympias deposit, and to evaluate the similarities and differences with other carbonate-hosted replacement deposits, discussed later in the paper. Assay data were collected from 2,690 exploration and production drill holes within 2 km north and south of the Stratoni fault zone, and 1,103 drill holes from the Olympias deposit area. The database was sorted by element (Ag, As, Au, Sb, Mn, Cu, Pb, and Zn) and filtered based on intercepts that were logged by company geologists as mineralized. Metal grades determined from this dataset are not based on economic factors and are therefore not necessarily representative of the measured and indicated resource estimates reported earlier (Eldorado Gold Corporation, 2017a). Assay data from the Stratoni fault zone and the Olympias deposit are plotted in three-dimensional sections as metal ratios in order to illustrate spatial trends (Figs. 4, 5). The objective of this study is to map district- and deposit-scale metal zonation patterns that may be indicative of hydrothermal fluid source(s) and direction of fluid flow within the Stratoni fault zone and around the Olympias deposit.

Elemental zoning is evident within the Stratoni fault zone, from Madem Lakkos in the east to Mavres Petres and Piavitsa in the west. On average, Pb and Zn grades are highest at the Mavres Petres deposit and lowest at the Piavitsa prospect. However, the Pb/Zn ratio decreases westward from the Madem Lakkos deposit to the Mavres Petres deposit (Fig. 4A) with the lowest values occurring in the east at the Piavitsa prospect. Silver correlates positively with Pb at both Madem Lakkos ($r = 0.84$) and Mavres Petres ($r = 0.94$). A decreasing trend in the Ag/Au ratio is evident from Madem Lakkos to the Mavres Petres deposit (Fig. 4B) with a minimum at the Piavitsa prospect. The replacement sulfide orebodies of the Madem Lakkos deposit contain about 0.60% Cu, whereas the average Cu grades at the Mavres Petres deposit and Piavitsa prospect are markedly lower at 0.04% and 0.02%, respectively. Arsenic

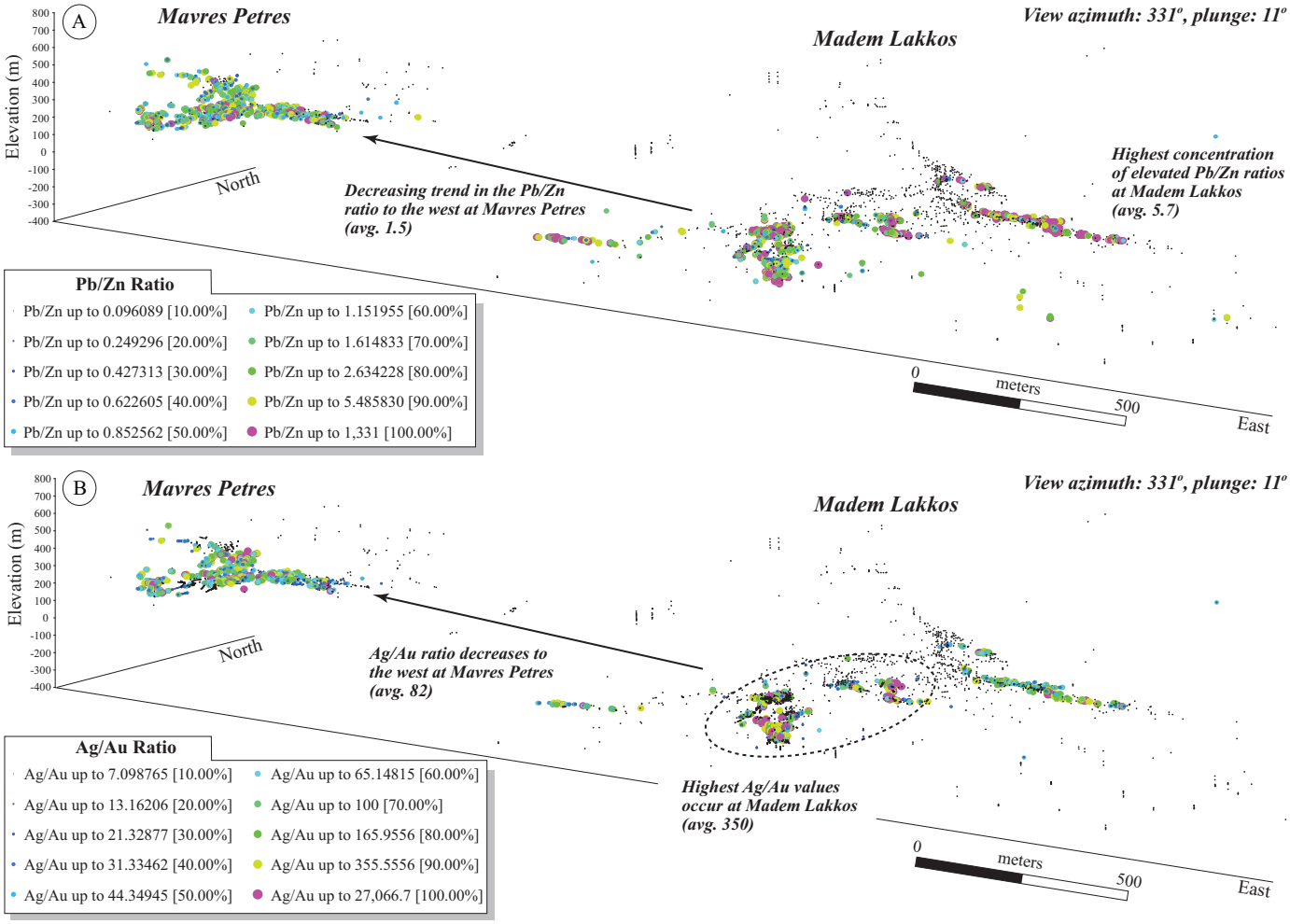

Fig. 4. Longitudinal view of the Stratoni fault zone displaying drill core geochemical assay data from the Madem Lakkos and Mavres Petres deposits, illustrating (A) Pb/Zn ratio and (B) Ag/Au ratio.

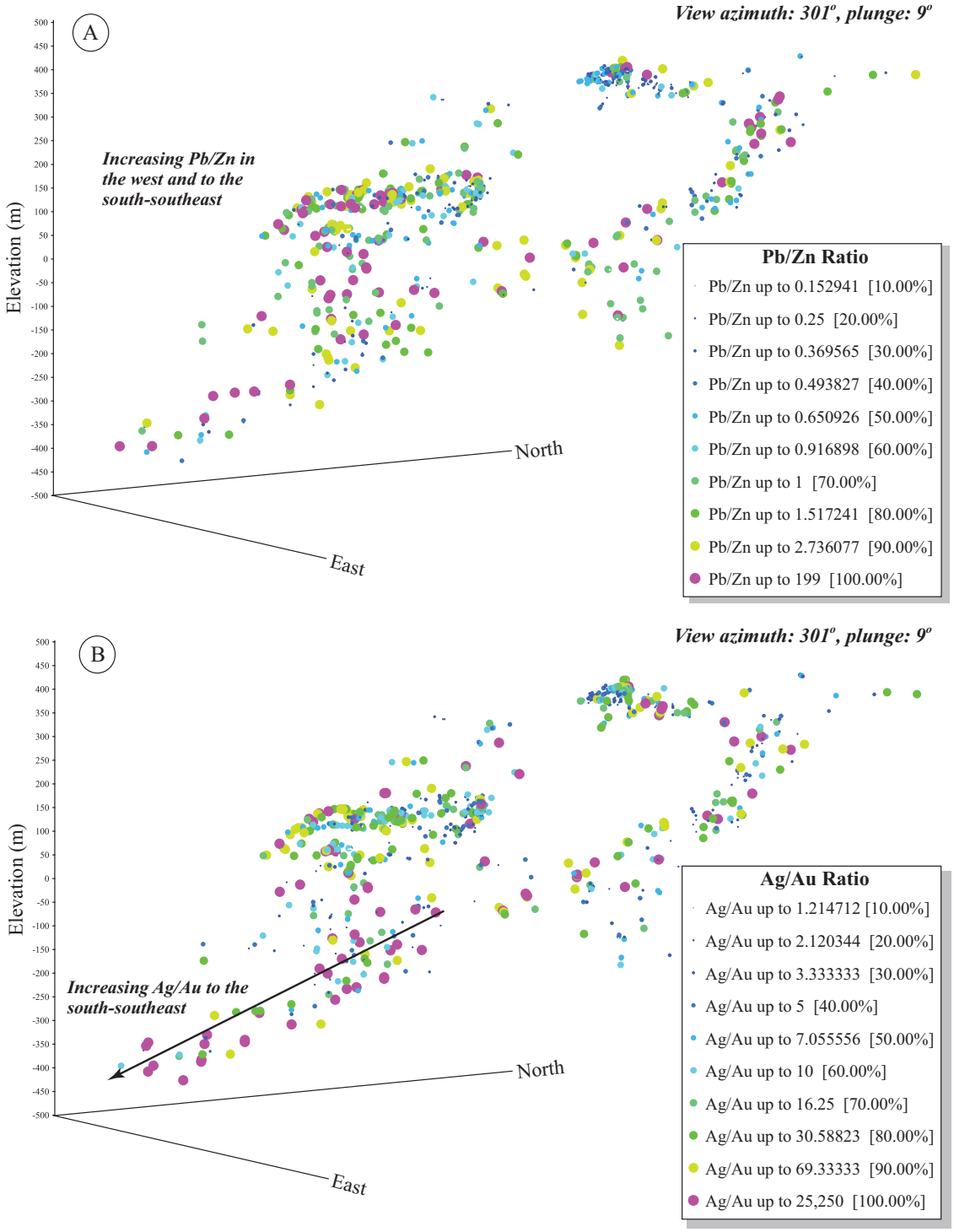

Fig. 5. Oblique cross-sectional view of the Olympias deposit displaying drill core geochemical assay data: (A) Pb/Zn ratio and (B) Ag/Au ratio.

and Sb were not systematically analyzed in the historic drilling from Madem Lakkos and Mavres Petres; therefore, modeling their distributions at the scale of the Stratoni fault zone was not possible. Assays for Mn from the Madem Lakkos deposit are limited, and Mn data from the Mavres Petres and Piavitsa areas are not sufficiently different to define spatial trends.

Metal zonation patterns are also evident at the Olympias deposit. Lead concentrations increase at depth toward the south-southeast, as illustrated by the Pb/Zn ratio in Figure 5A. Elevated Ag values also increase at depth and closely mimic Pb concentrations ($r = 0.95$). The Ag/Au ratio similarly increases with depth whereas Au is elevated in the upper

parts of the Olympias deposit (Fig. 5B) and corresponds positively with As (r = 0.81). Elevated Cu values characterize the upper northeast sector of the Olympias deposit where the sulfide ore lenses contain 0.04% Cu, on average. Similar to the Madem Lakkos deposit, Cu was not routinely analyzed historically, and its deposit-scale distribution remains tentative. The upper northwest portion of the Olympias deposit also appears to be enriched in antimony; however, Sb was not reported in many of the historic assays. Consequently, the distribution of Sb at the deposit scale is also uncertain.

Fluid Inclusion Microthermometry

Fluid inclusion microthermometry can aid in understanding the conditions of ore formation (Roedder, 1979) and was undertaken as part of this study to assist in developing a fluid flow zonation model for the carbonate replacement sulfide deposits in the district. Data presented here expand on previous work and add new results from the Olympias and Mavres Petres deposits and the Piavitsa prospect, particularly to evaluate the younger stages of carbonate replacement mineralization. Temperatures derived from fluid inclusion analyses are utilized in the modeling and interpretation of carbon and oxygen isotope results. Fluid inclusion data from earlier studies specific to the carbonate replacement deposits in the district are summarized below and are considered in the interpretation of data from this study. In the three aforementioned study sites, microthermometric measurements were conducted on fluid inclusions that exhibit only primary textures as defined by Roedder (1984), including those defining crystal growth zones, occurring as isolated inclusions or as isolated clusters of inclusions, or ones that contain an optically observable solid. Fluid inclusions that occur along recognizable healed fractures (e.g., secondary origin) were avoided. Analytical methodology, salinity calculation methods, and microthermometric data are presented in the digital Appendix.

Previous studies

Previous fluid inclusion studies from the Kassandra mining district have focused on the skarn and carbonate replacement sulfide orebodies at the Madem Lakkos and Olympias deposits (Kilias and Kalogeropoulos, 1989; Nebel et al., 1991; Gilg, 1993; Kilias and Madsen, 1994; Kilias et al., 1996), base metal-rich quartz-carbonate veins distal to the Madem Lakkos deposit and igneous quartz contained within the late Oligocene Stratoni granodiorite stock (Gilg, 1993), and the porphyry-style veins associated with the Skouries Au-Cu deposit (Frei, 1992, 1995; McFall, 2016). Previous microthermometric studies at the Olympias deposit were performed on primary and pseudosecondary fluid inclusions contained in quartz associated with sulfide ore (Kilias and Kalogeropoulos, 1989; Kilias and Madsen, 1994; Kilias et al., 1996). In the previous studies, three fluid inclusion types were defined. Fluid inclusion data presented in these studies were categorized based on sulfide morphology (e.g., Kalogeropoulos et al., 1989) rather than sulfide paragenesis; consequently, it is unclear which stage of sulfide mineralization their data represent. In the Madem Lakkos study, Gilg (1993) investigated primary and pseudosecondary fluid inclusions associated with skarn, massive sulfide, and disseminated sulfide styles of mineralization, which resulted in the classification of three major fluid inclusion types. Fluid inclusion subtypes were classified at both deposits, but these are considered minor deviations from the main populations. Photomicrographs of representative fluid inclusion types identified in the present study are shown in Figure 6. Data from previous work are displayed graphically in Figure 7 together with results from this study.

Microthermometric results

Olympias deposit: Fluid inclusions from the quartz-rich replacement sulfide lenses intercepted in drill core were evaluated from the Olympias deposit (Fig. 3D). Two samples investigated contain variable pyrite-galena-sphalerite and arsenopyrite with boulangerite interstitial to euhedral interlocking quartz grains. Euhedral and prismatic quartz is generally clear but commonly exhibits clouded growth zones defined by concentrations of submicron-scale fluid inclusions, most of which are unsuitable for microthermometric analysis. Previous work described fluid inclusion types from the replacement sulfide orebodies (Kilias and Madsen, 1994; Kilias et al., 1996); however, it was unclear if the paragenetically younger mineralization styles were included in their studies. Two primary fluid inclusion types were identified in quartz associated with sulfide. Type-1 fluid inclusions, defined here, may exhibit euhedral, negative-crystal forms (Fig. 6A) but are commonly elliptical to irregular in shape and are typically less than about 20 μm in length. These inclusions contain two phases consisting of aqueous liquid and vapor, the latter comprising of 30 to 40% of the inclusion at 25°C (Fig. 6A). Small transparent solids were observed in a few inclusions. A second type of fluid inclusion (type 2) occurs as clusters in proximity to type-1 inclusions and exhibits flat to elongate shapes that range from less than 5 μm to about 30 μm in their long dimension. At room temperature, two phases are present in the type-2 inclusions, consisting of aqueous liquid H_2O and a CO_2 vapor phase that occupies approximately 60% of the inclusion at 25°C (Fig. 6B). A volume of about 43% was determined using the equation of state for CO_2-bearing inclusions (Steele-MacInnis, 2018), thus suggesting that the observed CO_2 volume may be overestimated. All but two of the type-2 inclusions observed contain a small trapped transparent solid; however, the mineralogy of the solid phase is unknown.

Microthermometry of type-1 fluid inclusions yielded total homogenization temperatures that range from 227.8° to 365.6°C with an average of 309.6° ± 31.2°C (1σ; Fig. 7A). Final ice melting temperatures range from –5.8° to –1.4°C, yielding an average calculated salinity of 6.4 ± 2.0 wt % NaCl equiv (1σ; Fig. 7B). All but one type-2 fluid inclusions homogenize to the vapor phase within a narrow range of temperatures from 345.2° to 347.1°C (Fig. 7A). An array consisting of three type-2 inclusions, shown in Figure 6B, exhibits direct evidence for fluid immiscibility within the H_2O-CO_2-NaCl system, where two of the type-2 inclusions homogenize to vapor and one homogenizes to liquid (Fig. 6C). Such fluid immiscibility can yield information on the temperature and pressure of trapping given the known position of the H_2O-CO_2-NaCl solvus in pressure-temperature space. This is discussed further in a later section. Upon cooling from 25°C, the CO_2-rich portion of type-2 inclusions undergo phase separation such that liquid CO_2 forms a thin film coating

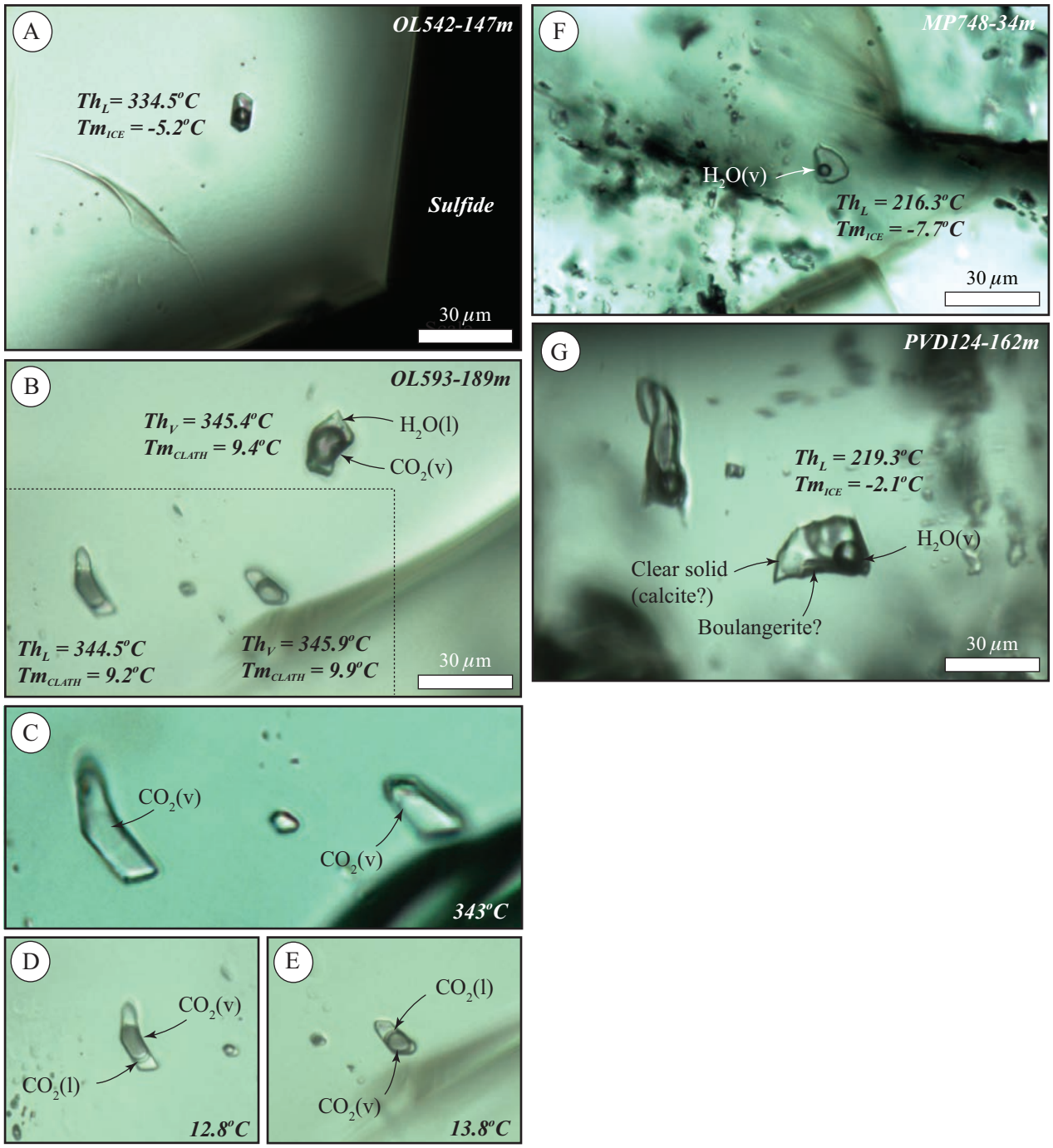

Fig. 6. Photomicrographs of representative primary fluid inclusions contained in quartz from the quartz-rich sulfide assemblage at the Olympias and Mavres Petres deposits and quartz-carbonate veins at the Piavitsa prospect. Microthermometric measurements are indicated on each image. A) Type-1 fluid inclusion in quartz from the Olympias deposit imaged at 25°C. (B) Type-2 fluid inclusions imaged at 25°C, trapped at slightly different focal levels in quartz, contain three phases in the system H_2O-CO_2-NaCl. Bimodal total homogenization behavior is indicated by expansion of the CO_2 bubble to the vapor phase (Th_v) and by shrinking of the CO_2 bubble to the liquid phase (Th_L). C) Photomicrograph of fluid inclusions outlined in image B taken at 343°C, near the homogenization temperature. Note shrinking of the CO_2 vapor bubble in the inclusion on the left and expansion of the CO_2 vapor bubble in the inclusion on the right. D, E) Photomicrographs of fluid inclusions outlined in image B taken at 12.8° and 13.8°C, documenting the presence of CO_2 liquid forming a meniscus on the CO_2 vapor bubble. F) Type-1 fluid inclusion in quartz from the Mavres Petres deposit imaged at 25°C. G) Type-1 fluid inclusion in quartz-rhodochrosite vein from the Piavitsa prospect imaged at 25°C. Note the presence of a clear crystal and needle-shaped opaque mineral interpreted to be trapped solid phases of calcite (?) and boulangerite, respectively. Abbreviations: l = liquid, Th_L = total homogenization temperature to the liquid phase, Th_V = total homogenization to the vapor phase, Tm_{CLATH} = final melting temperature of clathrate, Tm_{ICE} = final melting temperature of H_2O ice, v = vapor.

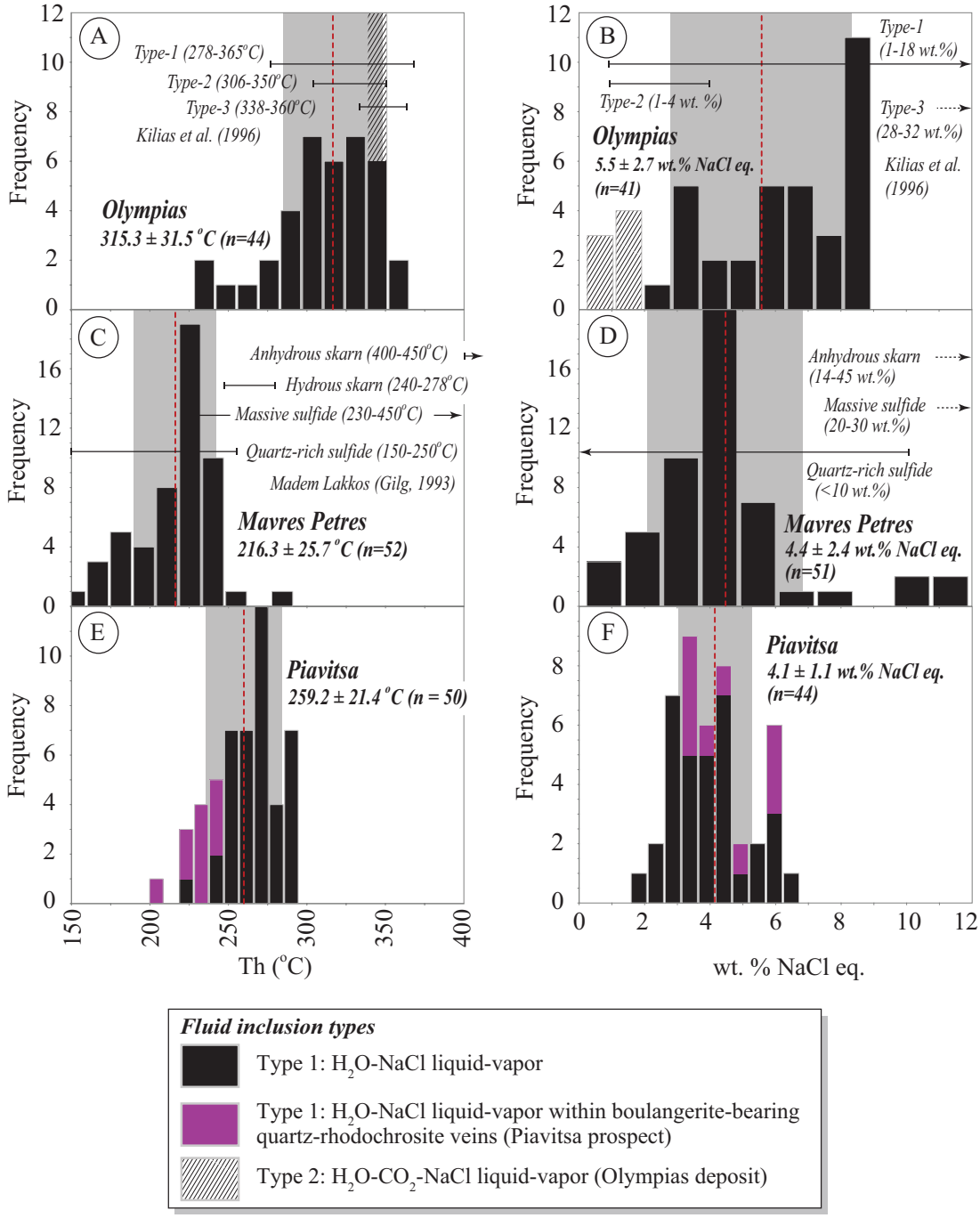

Fig. 7. Histograms of fluid inclusion microthermometric data showing total homogenization temperature (Th) (left) and calculated salinity (right) for primary fluid inclusions contained within quartz associated with quartz-rich replacement sulfide from the Olympias deposit (A, B), the Mavres Petres deposit (C, D), and the quartz-carbonate veins at the Piavitsa prospect (E, F). Average values and 1σ standard deviations for all measurements (type-1 and type-2 fluid inclusions) are shown in bold text and represented by the dashed red line and gray bounding box, respectively. Published homogenization temperature and salinity ranges for the Olympias and Madem Lakkos deposits are represented by horizontal bars in images A, B, C, and D.

the CO_2 vapor bubble between –7.5° and 17.2°C; the higher temperature is approximately where liquid CO_2 homogenizes into the CO_2 vapor phase. Figure 6D and E shows the presence of liquid CO_2 in two separate inclusions at 12.8° and 13.8°C. The final melting temperature of the solid CO_2 phase occurs from –57.7° to –56.9°C, below the triple point of pure CO_2 (–56.6°C), indicating the presence of a trapped gas other than CO_2 (e.g., Roedder, 1984). Final clathrate melting temperatures were measured from 9.2° to 9.9°C, yielding calculated salinities that range from 0.2 to 1.6 wt % NaCl equiv (Fig. 7B).

Mavres Petres deposit: Quartz gangue associated with replacement sulfide at the Mavres Petres deposit did not yield fluid inclusions amenable for microthermometric study.

However, boulangerite-bearing quartz-rich sulfide that displays textural and mineralogical similarities to the younger style of mineralization at the Olympias deposit was evaluated. Two samples were collected—one from drill core and another from an underground exposure at the 264-m level of the Mavres Petres mine (Fig. 3J). Each sample displays a distinctive interlocking network of euhedral and prismatic quartz intergrown with pyrite and sphalerite. A fibrous mesh of boulangerite and fine-grained secondary quartz infills open space between preexisting quartz grains (Fig. 3K). Coeval boulangerite and quartz also occupy fractures within earlier-deposited sulfide.

Analysis of primary fluid inclusions in synmineral quartz revealed type-1 inclusions, similar to those defined above at the Olympias deposit. Type-1 fluid inclusions are generally elliptical to irregular in shape and range from less than 5 to about 40 μm in length. At room temperature, these inclusions contain an aqueous liquid phase and a vapor phase that occupies 20 to 40% of the inclusion (Fig. 6F). Trapped solids are uncommon but may include transparent crystals and/or needle-shaped opaque crystals interpreted as carbonate daughter minerals and boulangerite, respectively. Type-1 fluid inclusions display homogenization temperatures that range from 144.7° to 291.6°C with an average of 216.3° ± 25.7°C (1σ; Fig. 7C). Several fluid inclusions recorded lower homogenization temperatures and are interpreted as inclusions that have undergone postentrapment modification. Salinities calculated from final ice melting temperatures range from 0.9 to 11.9 wt % NaCl equiv with an average of 4.4 ± 2.4 wt % NaCl equiv at 1σ variation. A subset of type-1 inclusions displays salinities >10 wt % NaCl equiv (Fig. 7D).

Piavitsa prospect: Two drill core samples from base metal-rich quartz-calcite veins containing sphalerite-pyrite-galena-arsenopyrite were analyzed (Fig. 3M). These veins exhibit a distinctive pale green mica-quartz-carbonate-pyrite alteration envelope that also occurs near the replacement sulfide lenses at the Mavres Petres and Olympias deposits. A boulangerite-bearing quartz-rhodochrosite vein intercepted in drill core was also analyzed (Fig. 3P), although the timing between the two vein styles is uncertain. The quartz-rhodochrosite vein contains clear quartz exhibiting a zoned and crustiform texture with black chalcedonic quartz that hosts minor sphalerite and pyrite with abundant boulangerite. Fluid inclusions contained within the black chalcedonic quartz are generally <5 μm and unsuitable for microthermometric analysis; consequently, primary fluid inclusions within the coarser-grained clear quartz were examined.

Microthermometry of quartz from the base metal-rich quartz-calcite and the quartz-rhodochrosite veins revealed only type-1 fluid inclusions, similar to those defined above. Type-1 fluid inclusions from both vein styles are elliptical to elongate in shape and commonly exceed about 30 μm in length (Fig. 6G). Type-1 fluid inclusions contain two phases, consisting of aqueous H_2O liquid and a vapor phase typically occupying 20 to 40% of the inclusion. Some inclusions contain needle-shaped opaque solids and euhedral clear crystals that are interpreted to be boulangerite and carbonate daughter minerals based on their crystallographic forms. Type-1 fluid inclusions in the base metal-rich quartz-calcite veins homogenize to the liquid phase at temperatures ranging from 226.5° to 294.9°C, yielding an average temperature of 266.6° ± 16.0°C (1σ; Fig. 7E). Fluid inclusions contained in quartz-rhodochrosite veins similarly homogenize to the liquid phase, but at lower temperatures ranging from 199.3° to 239.7°C, which average 229.4° ± 12.3°C (1σ; Fig. 7E). Final ice melting temperatures for both vein styles correspond to calculated salinities that span 1.6 to 6.7 (average 4.1 ± 1.1 at 1σ variation) wt % NaCl equiv (Fig. 7F).

Carbon and Oxygen Stable Isotopes

Carbon and oxygen stable isotopes are geochemical tracers that can be used to understand the nature, evolution, and flow of hydrothermal fluids in carbonate environments (e.g., Engel et al., 1958). This study presents the results of 234 coupled carbon-oxygen isotope measurements of carbonate that were determined using a laser infrared absorption technique based on off-axis integrated cavity output spectroscopy (OA-ICOS). The detailed methodology of OA-ICOS and comparisons with conventional isotope ratio mass spectroscopy (IRMS) are described in Barker et al. (2011) and Beinlich et al. (2017). The objective of the stable isotope study was to investigate the district-scale zonation pattern recorded in gangue and wall-rock marble and to model the processes that controlled the isotopic composition of carbonate minerals associated with the replacement systems in the Stratoni fault zone and in the Olympias area. Carbon-oxygen isotope data are presented in standard δ-notation and displayed on conventional $\delta^{13}C$ vs. $\delta^{18}O$ covariation diagrams. Isotopic patterns exhibited by carbonate occurring as marble, gangue associated with sulfide ore, and vein breccias are described with respect to their mineralogy as determined from a qualitative staining technique that uses a dilute hydrochloric acid solution containing alizarin red S and potassium ferricyanide (Hitzman, 1999). Theoretical mass balance calculations that describe the effect of fluid-rock interaction and decarbonation reactions (Taylor, 1974, 1979; Valley, 1986; Bowman, 1998; Baumgartner and Valley, 2001) are presented in the discussion section. Sampling procedures, analytical methodology, model calculations, and carbon-oxygen isotope data are located in the digital Appendix.

Previous studies

Stable isotope studies have been previously performed on the marble host rocks and carbonate minerals associated with the replacement sulfide orebodies from the Madem Lakkos and Olympias deposits (Kalogeropoulos and Kilias, 1989; Kalogeropoulos et al., 1989; Gilg, 1993). Low $\delta^{18}O$ values from marble and ore-related gangue carbonate at the Olympias deposit led Kalogeropoulos et al. (1989) to conclude that isotopic exchange resulted from water-dominated fluid-rock interaction rather than CO_2 decarbonation processes. Gilg (1993) similarly reported low $\delta^{18}O$ values in marble and gangue associated with the sulfide orebodies at the Madem Lakkos deposit; however, the mechanism that controlled isotope depletion was not discussed. Hahn (2014) conducted a marble provenance study using carbon and oxygen isotopes collected from the Olympias, Mavres Petres, and Piavitsa areas, but an insufficient number of samples (n = 7) precluded definitive conclusions. Published carbon and oxygen isotope data from unaltered marble to the north of the Kassandra mining district are probably representative of the isotopic background of

Permo-Carboniferous marble in the region (Varti-Matarangas and Eliopoulos, 2005; Boulvais et al., 2007; Eliopoulos and Kilias, 2011) and are shown as blue diamonds in Figure 8A and illustrated by the blue boxes in each subsequent diagram.

Carbon and oxygen isotope composition of marble and hydrothermal carbonates

Olympias deposit: Carbon and oxygen stable isotope ratios were determined from marble, carbonates in contact with stylolites within the hosting marble, coarse-grained carbonate spar associated with replacement sulfide, and late-stage quartz-rhodochrosite vein breccias (Fig. 8A-C). The Olympias marble mostly consists of calcite, which exhibits a wide distribution of $\delta^{13}C$ and $\delta^{18}O$ values ranging from +2.4 to –6.3‰ and 31.3 to 6.1‰, respectively (Fig. 8A). Carbonate minerals contacting stylolites within about 10 m from known sulfide ore show a restricted range of $\delta^{13}C$ (0.8–0.3‰) and $\delta^{18}O$ values (28.3–22.4‰; Fig. 8B). Euhedral, coarse-grained gangue carbonate minerals associated with replacement sulfide consist mostly of calcite and rhodochrosite, as shown in Figure 8B. Calcite $\delta^{13}C$ values range from +2.3 to –0.8‰ with $\delta^{18}O$ values spanning 26.7 to 3.0‰. Rhodochrosite $\delta^{13}C$ and $\delta^{18}O$ values are also depleted, ranging between +1.5 and –2.2‰ and 17.5 and 10.1‰, respectively (Fig. 8B). Rhodochrosite, ferroan calcite, and calcite characterize the carbonate mineral species associated with the paragenetically younger vein breccias at the Olympias deposit. Vein-related rhodochrosite exhibits a wide range of $\delta^{13}C$ values from +2.6 to –1.9‰ and $\delta^{18}O$ values between 16.9 and 8.7‰ (Fig. 8C). The mean $\delta^{18}O$ value for vein rhodochrosite is broadly similar to that of the coarse-grained rhodochrosite associated with replacement sulfide. Ferroan calcite veins, however, vary widely with $\delta^{13}C$ values ranging from +2.0 to –2.4‰ and $\delta^{18}O$ values spanning from 17.7 to 4.6‰. A single vein sample composed of calcite yielded a similar $\delta^{13}C$ (0.2‰) and $\delta^{18}O$ (15.6‰) composition.

Deposits within the Stratoni fault zone: Carbon and oxygen stable isotope compositions were similarly determined for marble, carbonates at the margins of stylolites, gangue carbonate minerals associated with skarn and replacement sulfide ore, and late-stage quartz-rhodochrosite vein breccias from the Madem Lakkos and Mavres Petres deposits and the Piavitsa prospect (Fig. 8D-F). Marbles within the Stratoni fault zone are predominantly composed of calcite with minor ferroan calcite and rhodochrosite (Fig. 8D). Marble exhibits $\delta^{13}C$ and $\delta^{18}O$ values that vary from +3.2 to –2.8‰ and 30.5 to 3.2‰, respectively. Carbonates occurring at stylolite margins exhibit a wide range of $\delta^{13}C$ (+1.6 to –2.0‰) and $\delta^{18}O$ (21.8–5.9‰) values as shown in Figure 8E. Carbonate minerals associated with skarn and replacement sulfide at the Madem Lakkos and Mavres deposits exist as calcite, ferroan species of calcite and dolomite, and rhodochrosite. Skarn-related carbonates have a large range of $\delta^{13}C$ values from +0.4 to –2.9‰ and a restricted $\delta^{18}O$ distribution from 16.0 to 10.0‰. Carbonates occurring with replacement sulfide have a similar range of isotopic compositions, particularly for oxygen ($\delta^{13}C$ = +1.9 to –2.5‰ and $\delta^{18}O$ = 17.1–7.8‰; Fig. 8E). Carbonate minerals associated with vein breccias also display diverse mineralogy consisting of rhodochrosite and calcite, including ferroan varieties of calcite and dolomite. Quartz-carbonate vein breccias exhibit a broad range of $\delta^{13}C$ values spanning +3.3 to –3.2‰, with low $\delta^{18}O$ values from +14.4 to –6.0‰ (Fig. 8F).

Lead Isotopes

Lead isotopes can provide important information on the metal source, wall rock or intrusions, and the pathway of hydrothermal fluids that resulted in the deposition of sulfide ore (Tosdal et al., 1999). The principal objective of the Pb isotope study is to determine whether the Pb isotope compositions of the sulfide orebodies correlate with an igneous intrusion (or intrusions) in the district, and whether the Pb isotope composition in the sulfide bodies within the Stratoni fault zone changes with distance from the major intrusive centers, potentially identifying a source of ore fluids. While Pb isotope studies have been conducted previously in the district (Chalkias and Vavelidis, 1989; Mantzos, 1989; Nebel et al., 1991; Frei, 1992, 1995), reevaluation is justified in the context of the revised regional- and deposit-scale geologic framework reported in Siron et al. (2016, 2018). This section presents the results of six igneous feldspar samples collected from the late Oligocene Stratoni granodiorite stock, early Miocene porphyry bodies in the Aspro Lakkos area, and a black-matrix porphyry dike in the Stratoni fault zone (Siron et al., 2016), including 10 sulfide samples from the Olympias, Madem Lakkos, and Mavres Petres deposits and the Piavitsa prospect. Lead isotope data are displayed on conventional $^{207}Pb/^{204}Pb$ vs. $^{206}Pb/^{204}Pb$ and $^{208}Pb/^{204}Pb$ vs. $^{206}Pb/^{204}Pb$ diagrams together with the two-stage Pb evolution curves of Stacey and Kramers (1975) and Chalkias and Vavelidis (1989). The latter is a plumbotectonics model that describes the evolution of Pb specific to north Aegean crust. Results described hereafter will be in reference to the latter model curve. Analytical methodology, sample locations, and Pb isotope data are located in the digital Appendix.

Previous studies

Previous work in the district has contributed a wealth of Pb isotope data from the metamorphic basement rocks, carbonate replacement sulfide ore and sulfide associated with the Skouries deposit, and the late Oligocene and early Miocene intrusive suites. This comprehensive database permits interpretation of potential source reservoirs for Pb. Frei (1992, 1995) determined the Pb isotope composition of the Vertiskos and Kerdilion units in the Skouries and Olympias areas, respectively, based on plagioclase and whole-rock analyses. Analyses from an amphibolite body outcropping south of the Stratoni fault zone (Fig. 2) were also reported. These data are plotted as stippled fields in Figure 9A to D. Lead isotope data from the Stratoni granodiorite stock plot in the field that defines the Kerdilion unit (Fig. 9A, B), whereas the monzodiorite and granodiorite bodies in the Tsikara and Fisoka areas (Fig. 2) mostly plot in the field of overlapping metamorphic basement units. Analyses from the early Miocene igneous suite, which includes the Skouries and Aspro Lakkos porphyry stocks, black-matrix porphyry dikes that occur in the Aspro Lakkos and Tsikara areas (Fig. 2), and a black-matrix porphyry dike at the Madem Lakkos deposit, display a restricted range of Pb isotope ratios that mostly plot in the field defining the Vertiskos unit (Fig. 9A, B). Sulfide Pb isotope compositions of galena previously reported for the Olympias, Madem Lakkos, and Mavres Petres deposits (Chalkias and Vavelidis, 1989; Kalogeropoulos

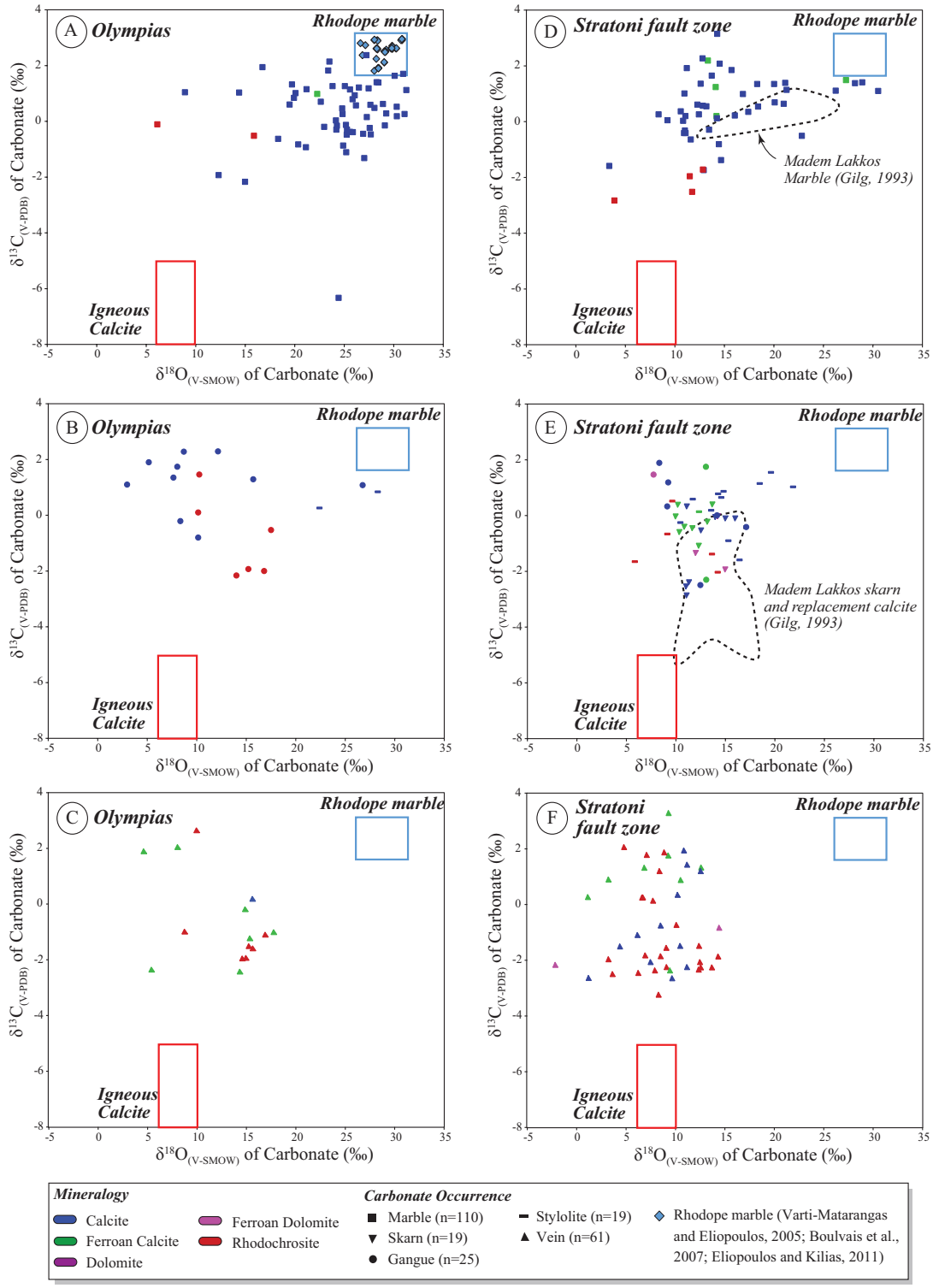

Fig. 8. Plots of $\delta^{13}C_{V\text{-}PDB}$ vs. $\delta^{18}O_{V\text{-}SMOW}$ reported in ‰ for carbonate phases associated with the carbonate replacement deposits from the Kassandra mining district. Carbonate data are displayed with respect to mineralogy and style of occurrence. The fields for igneous calcite (Bowman, 1998; Hoefs, 2004) and unaltered Rhodope marble (Varti-Matarangas and Eliopoulos, 2005; Boulvais et al., 2007; Eliopoulos and Kilias, 2011) are illustrated on each diagram. Carbon and oxygen isotope data from the Olympias deposit are plotted with respect to marble host rock (A), gangue carbonate minerals associated with replacement sulfide and stylolitic fluid escape structures (B), and quartz-rhodochrosite vein breccias (C). Data from the Stratoni fault zone are displayed with respect to marble host rock (D), gangue carbonate minerals associated with replacement and skarn sulfide and stylolitic fluid escape structures (E), and quartz-rhodochrosite vein breccias (F). Values reported in Gilg (1993) are illustrated by the dotted lines. Abbreviations: V-PDB = Vienna-Pee Dee Belemnite, V-SMOW = Vienna-Standard Mean Ocean Water.

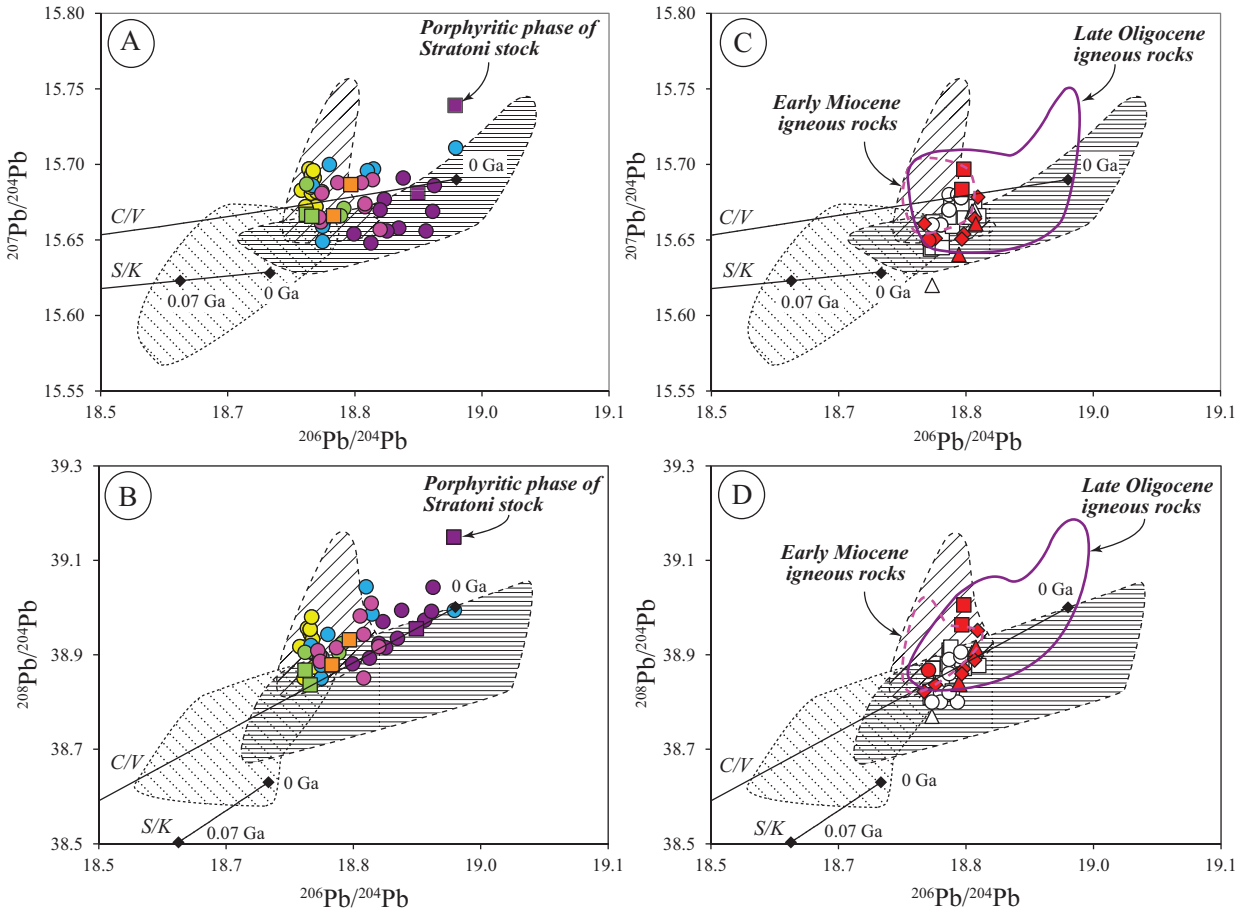

Igneous Rocks: K-feldspar
(Legend for Fig. 9A-B)

- ○ Published data (Frei, 1992; Nebel, 1989)
- □ This study

Early Miocene porphyry stocks and dikes

- Vathilakkos black-matrix porphyry dike
- Aspro Lakkos porphyry stock & black-matrix porphyry dike
- Skouries quartz monzonite porphyry stock, megacrystic K-feldspar porphyry dike

Late Oligocene stocks and dikes

- Fisoka granodiorite-diorite stock and adjacent porphyry dikes
- Stratoni granodiorite stock
- Tsikara monzodiorite

Metamorphic Basement Rocks (Frei, 1992, 1995)

- Biotite and amphibole-bearing biotite gneiss from the Skouries and Aspro Lakkos areas (Vertiskos unit)
- Amphibolite from the Gomati and Stratoni mafic and ultramafic bodies
- Biotite gneiss and amphibolite from the Olympias and Madem Lakkos areas (Kerdilion unit)

Sulfide: galena and pyrite
(Legend for Fig. 9C-D)

- ○ Published data (white polygons and circles: Chalkias and Vavelidis, 1989; Kalogeropoulos et al., 1989; Nebel, 1989)

This study

- ■ Madem Lakkos skarn (pyrite)
- ▲ Mavres Petres massive sulfide (galena)
- ● Olympias massive sulfide (galena)
- ◆ Piavitsa semi-massive sulfide (galena and pyrite)

Fig. 9. Lead isotope data are displayed on conventional $^{207}Pb/^{204}Pb$ vs. $^{206}Pb/^{204}Pb$ and $^{208}Pb/^{204}Pb$ vs. $^{206}Pb/^{204}Pb$ diagrams. The two-stage crustal Pb evolution curves of Stacey and Kramers (1975) and Chalkias and Vavelidis (1989) are shown for reference and labeled S/K and C/V, respectively. The stippled and lined fields corresponding to Pb isotope compositions of the metamorphic basement units are adapted from Frei (1992, 1995). (A, B) Lead isotope values of Oligo-Miocene igneous rocks from this study are displayed as squares with data from Frei (1992) displayed as circles; (C, D) lead isotope compositions of galena and pyrite from this study are displayed in red with published data shown in white (Chalkias and Vavelidis, 1989; Nebel, 1989; Kalogeropoulos et al., 1989). The dashed pink and solid purple shapes correspond to the ranges of early Miocene and late Oligocene igneous rocks, respectively.

et al., 1989; Nebel, 1989; Nebel et al., 1991) are isotopically uniform, largely correlating to the field defined by overlapping metamorphic basement units, as well as the igneous feldspar and whole-rock Pb isotope compositions that characterize the Oligo-Miocene igneous rocks within the district (Fig. 9C, D).

Lead isotope compositions of igneous feldspars and sulfide minerals

Igneous feldspars: Primary K-feldspar phenocrysts from two samples of the late Oligocene Stratoni stock were analyzed for their Pb isotope composition. These samples correspond to zircon U-Pb ages of 25.4 ± 0.2 Ma from the main equigranular granodiorite body and 24.5 ± 0.3 Ma for a porphyritic granodiorite phase located at the northern and topographically highest portion of the intrusive stock (Fig. 2; Siron et al., 2016). The Pb isotope composition of the equigranular granodiorite phase agrees with previously published results from the Stratoni stock (Frei, 1992). The porphyritic granodiorite phase, however, plots well above the north Aegean crustal growth curve and other Pb isotope ratios from the Oligo-Miocene suite (Fig. 9A, B), indicating that this intrusive phase is distinct from the equigranular granodiorite and the Kerdilion unit that host the Stratoni stock. Lead isotope ratios were also obtained from three early Miocene porphyry samples previously dated by zircon U-Pb methods (Siron et al., 2016). Primary K-feldspar phenocrysts were analyzed from the 19.7 ± 0.1 Ma megacrystic K-feldspar porphyry stock and a crosscutting 19.6 ± 0.1 Ma black-matrix porphyry dike in the Aspro Lakkos area, as well as the 19.2 ± 0.2 Ma black-matrix porphyry dike hosted by the Vathilakkos fault above the Madem Lakkos deposit (Fig. 2). Lead isotope compositions cluster within the field of overlapping metamorphic basement units (Fig. 9A, B), consistent with published data from the Skouries porphyry stock and porphyry dikes elsewhere in the district (Frei, 1992, 1995).

Sulfide minerals: Lead isotope ratios from galena associated with skarn at the Madem Lakkos deposit plot above the north Aegean crustal growth curve and correspond to the field defined by the Vertiskos unit. Skarn-related sulfide, however, is hosted by Kerdilion marbles (Fig. 9C, D) and appears to contain more radiogenic Pb than the carbonate replacement sulfide. Galena and pyrite from sulfide at the Mavres Petres deposit and the Piavitsa prospect are isotopically similar and occur within the field of overlapping metamorphic basement units, as well as the overlapping field of late Oligocene and early Miocene igneous rocks (Fig. 9C, D). Galena Pb from the Olympias deposit is isotopically similar to Pb contained in sulfide from the Stratoni fault zone (Fig. 9C, D). Boulangerite from a quartz-rhodochrosite vein at the Piavitsa prospect was also analyzed to characterize the Pb associated with the latest stage of mineralization in the district. While the Pb isotope composition is coincident with the replacement sulfide data, large analytical errors preclude interpretation and it was therefore omitted.

Discussion

District-scale metal zonation as a vector for hydrothermal fluid flow and metal deposition

Distinct mineralogical and metal zonation patterns are evident in the deposits and between the zones of mineralization along the Stratoni fault zone. The southeastern part of the Madem Lakkos deposit is characterized by chalcopyrite-scheelite–bearing skarn spatially associated with aplitic sills. Subordinate skarn development in the gneisses adjacent to the Stratoni granodiorite could indicate that the fluids responsible for the Madem Lakkos skarn body were derived from the east (Fig. 2). Cubanite-chalcopyrite exsolution textures and abundant magnetite in the southeastern portion of the Madem Lakkos orebody were interpreted by Nicolaou (1964) as a high-temperature zone, possibly resulting from a blind intrusive source at depth or the Fisoka stock to the south (Fig. 2). While Cu is clearly present in the skarn at Madem Lakkos, assays of skarn bodies intersected in historic drilling do not routinely include Cu. Thus, it is likely either that Cu was not systematically assayed or that, if obtained, Cu assays were not transferred from the paper logs to the digital database. Assayed skarn intercepts reporting Au in the historic database from the Madem Lakkos deposit (n = 229) yielded an average Au grade of about 0.3 g/t with a range from trace to 5.1 g/t, indicating that the skarn bodies are relatively Au poor compared to replacement sulfide within the Stratoni fault zone (see discussion below). The mineralized skarn ore also contains minor concentrations of Pb and Zn (0.8% combined) at about equal proportion.

The transition from skarn into sphalerite-galena and pyrrhotite-bearing, pyrite-rich replacement massive sulfide bodies resembles the zonation sequence developed in many skarn and carbonate replacement deposits in central and northern Mexico (Megaw et al., 1988; Baker and Lang, 2003). Pyrrhotite may be indicative of a more reduced and high-temperature environment (e.g., Hemley and Hunt, 1992), consistent with fluid inclusion evidence from Madem Lakkos (Gilg, 1993). The highest Cu values in the non-skarn replacement sulfide orebodies within the Stratoni fault zone occur at the Madem Lakkos deposit. Copper is mostly contained in chalcopyrite, as individual grains or inclusions in sphalerite and pyrite, but also in tetrahedrite-tennantite (Nicolaou, 1964), which commonly forms inclusions within galena. Bournonite and enargite (Gilg, 1993) in the volumetrically more abundant and paragenetically younger quartz-rich sulfide assemblage additionally contribute to the elevated Cu grades in the Madem Lakkos deposit. In general, Cu diminishes toward the west with Pb and Zn concentrations increasing at the Mavres Petres deposit. The lower Pb/Zn ratio at Mavres Petres and Piavitsa relative to the Madem Lakkos sulfide ore indicates increased precipitation of Zn in the west of the Stratoni fault zone (Fig. 4A). This pattern conflicts with the solubility of Pb and Zn in hydrothermal fluids in rock-buffered systems as predicted by Hemley and Hunt (1992) and the observed metal zonation patterns in other carbonate replacement deposits (Megaw, 1990; Vikre, 1998). Multiple mineralizing stages as part of a single hydrothermal event may therefore explain the distribution of Zn within the Stratoni fault zone.

The Madem Lakkos massive sulfide bodies average 1.3 g/t Au, almost an order of magnitude higher than skarn-related sulfide. Gold markedly increases to the west, where the highest Au grades occur in the skarn-free replacement sulfide bodies at the Mavres Petres deposit (average 4.9 g/t Au; Fig. 4B). Many carbonate replacement deposits display elevated Au

concentrations in proximity to mineral-related intrusions. In the Leadville district of Colorado, the highest Au grades in the replacement sulfide orebodies (>6.8 g/t) occur adjacent the Breece Hill stock and in contact with faults that intersect the igneous body at depth (Thompson and Arehart, 1990). However, the distal environment may be enriched in Au, such as in the Bingham district of Utah. Disseminated Au hosted by carbonate rocks at Barneys Canyon, interpreted as being related to the Bingham Canyon porphyry system, implies dispersal of hydrothermal fluids for over 7.5 km from the intrusive center (Cunningham et al., 2004). The Mavres Petres deposit occurs about 2 to 3 km from the late Oligocene Stratoni and Fisoka stocks (Fig. 2), and the aplitic dikes and sills that are spatially associated with the sulfide ore at Madem Lakkos were not observed at the Mavres Petres deposit. While early Miocene glomerophyric porphyry dikes occur in the area, they clearly postdate the sulfide orebody (see Siron et al., 2016, 2018). The Au (As, Ag, Sb)–enriched sulfide bodies at the Mavres Petres deposit, therefore, either resulted from the efficient transport of Au in hydrothermal solution westward along the Stratoni fault zone or from hydrothermal fluids that were channelized directly from a nearby source intrusion at depth.

Silver and Mn grades generally increase toward the periphery of many intrusion-related carbonate replacement systems (Megaw, 1998). In the Leadville district, Thompson and Arehart (1990) showed a rise in Ag with a corresponding decrease in Au grade with increasing distance from the Breece Hill stock. However, the Mavres Petres deposit exhibits a modest increase in Ag but with markedly higher Au grades, which corresponds to a lower Ag/Au ratio than at the Madem Lakkos deposit (Fig. 4B). Silicified Mn-rich gossans that crop out above the Mavres Petres deposit and to the west in the Piavitsa area are the surface equivalent of quartz-rhodochrosite ± rhodonite replacement bodies at depth, and are representative of the vertical and lateral expression of the carbonate replacement system within the Stratoni fault zone. An analogous relationship of Mn-rich alteration outboard from the sulfide replacement orebodies is documented in the Tintic district of Utah (Morris and Lovering, 1979) and the Santa Eulalia camp of northern Mexico (Megaw et al., 1988). Manganese is rarely reported in the historic assays, particularly at the Madem Lakkos deposit. Consequently, outside of mineralogical observations, the drill core data are insufficient to define a zonal geochemical pattern for Mn within the Stratoni fault zone.

Deposit-scale metal zonation patterns evident at the Olympias deposit may also be used as a vector for hydrothermal fluid flow. The sulfide lenses that occur on the eastern portion of the deposit in association with ductile-brittle fault strands display the highest Cu values within the deposit and, along with anomalously high W and Mo contents, possibly suggest a higher-temperature fluid in proximity to an intrusive source. In general, the sulfide bodies at Olympias are enriched in Au, with the highest values focused along the Kassandra fault zone in the upper parts of the deposit. Silver and the Ag/Au ratio increase with depth toward the south-southeast (Fig. 5B), suggesting that the down-plunge extent of the Olympias orebody may be more distal from the hydrothermal fluid source. Manganese is elevated at shallow depths in the north and at the western, up-dip portion of the Kassandra fault; however, this may reflect cooling of hydrothermal fluid and/or supergene enrichment as a result of near-surface oxidation. Deposit-scale metal zonation patterns with elevated Cu-W-Mo in the east, homogenization temperatures exceeding 350°C, and the presence of synmineral granitic breccia dikes (Siron et al., 2018) all suggest that the Olympias orebody may have formed relatively close to an intrusive source, potentially located at depth and to the east of known mineralization.

The interpreted down-plunge and distal extent of the Olympias orebody, as inferred by the metal distribution patterns, is intriguing because the downward migration of buoyant hydrothermal fluid is unlikely. It is possible that this pattern is the product of deposit- or regional-scale fault block rotation and tilting of the orebody or convective circulation of a hydrothermal fluid confined to a lithologic horizon (e.g., marble) in the presence of a steep geothermal gradient. Provided this lithologic layer is dipping and sealed, hydrothermal fluid would be forced to migrate in a downward direction with respect to the paleosurface (Cathles, 1997). Alternatively, the metal zonation pattern of the Olympias deposit is probably best explained by two stages of mineralization, which is consistent with the observed timing relationship between early base metal-rich massive sulfide overprinted by the younger quartz-rich sulfide phase.

Constraints on pressure, temperature, and depth of deposit formation

Microthermometric data reveal a broad zonation pattern from east to west within the deposits hosted by the Stratoni fault zone. Published fluid inclusion data from the Madem Lakkos deposit (Gilg, 1993) revealed decreasing temperatures from ~450°C with deposition of early skarn and replacement massive sulfide to less than 278°C for retrograde skarn and 250°C for the late quartz-rich, disseminated sulfide event. Due to inadequate fluid inclusions, the conditions of early replacement sulfide at the Mavres Petres deposit were not determined and therefore require further work. The results of this study, however, show relatively low temperatures for the open-space, boulangerite-bearing, quartz-rich sulfide assemblage at the Mavres Petres deposit (~216°C), suggesting decreasing temperature with time and toward the west. The Au-bearing base metal-rich quartz-carbonate veins in the Piavitsa area probably belong to the early replacement sulfide phase as inferred from mineralogical similarities and elevated homogenization temperatures, whereas the lower-temperature, boulangerite-bearing quartz-rhodochrosite veins are similar in texture and mineralogy to the later quartz-rich sulfide.

At the Madem Lakkos deposit, Gilg (1993) documented CO_2-rich fluid inclusions that homogenized to the liquid and vapor phase, with a coexisting population of highly saline H_2O-rich inclusions containing upward of 45 wt % NaCl equiv. This relationship was previously interpreted to reflect fluid immiscibility resulting from the unmixing of a CO_2-rich parent fluid either by decarbonation reactions or due to a pressure drop in response to boiling (Gilg, 1993). Unmixing of a homogeneous fluid as a result of decarbonation is not supported by carbon-oxygen stable isotope models discussed later. While boiling as a mechanism for sulfide deposition is possible, the lack of fluid inclusion evidence, particularly within the younger

quartz-rich sulfide ore and quartz-rhodochrosite vein breccias at Mavres Petres and Piavitsa, precludes this interpretation. Processes considered more likely for replacement-style mineralization are fluid-rock interaction and/or fluid mixing. The high-salinity fluid inclusions reported at the Madem Lakkos deposit may also reflect one end-member of an immiscible magmatic fluid that was preserved close to its source and, while CO_2 may have originated from a magmatic fluid, dissolution of marble is a more likely CO_2 source (e.g., Ohmoto and Rye, 1979).

At the Olympias deposit, we observed no coexistence of highly saline H_2O-rich inclusions and CO_2-rich type-2 inclusions and, therefore, no evidence for H_2O-NaCl and H_2O-CO_2 immiscibility. There is direct evidence, however, of fluid immiscibility among type-2 inclusions. Within a single type-2 fluid inclusion array, two inclusions homogenize by vapor disappearance, while one inclusion homogenizes to the liquid phase (Fig. 6C). This homogenization behavior is interpreted as fluid immiscibility within the system H_2O-CO_2-NaCl, where the total homogenization temperature and pressure represent trapping conditions (Roedder, 1984). For this array, trapping temperatures were measured at about 345°C, whereas pressure was inferred from the position of the solvus in the system H_2O-CO_2-NaCl. The calculated salinities for the three inclusions shown in Figure 6B are between 0.2 and 1.6 wt % NaCl equiv. The position of the solvus is well known at 0 and 6 wt % NaCl (Tödheide and Franck, 1963; Gehrig, 1980), but, to our knowledge, no experimental data exist between these values. The position of the solvus in pressure-temperature space for 0 and 6 wt % NaCl and the inferred position of the solvus at 2 wt % NaCl are displayed in Figure 10 (modified after Schmidt and Bodnar, 2000). The immiscible fluid inclusion array shown in Figure 6B must have been trapped along the solvus somewhere between 0 and 2 wt % NaCl. As illustrated in Figure 10 at 345°C, the trapping pressure is estimated between about 15 and 58 MPa (150–580 bars). A trapping pressure of 522 bars was also determined using the equation of state for CO_2-bearing inclusions that homogenize to the liquid phase in the system H_2O-CO_2-NaCl (Steele-MacInnis, 2018). These results are broadly consistent with pressure estimates (<500 bars) reported in previous studies from the Olympias deposit (Kilias and Kalogeropoulos, 1989; Kilias and Madsen, 1994; Kilias et al., 1996).

Based on the inferred trapping pressures (Fig. 10), carbonate replacement mineralization at the Olympias deposit would correspond to an estimated depth ranging between 1.5 and 5.9 km, assuming fluid-dominated hydrostatic pressure conditions. The lack of evidence for boiling and an independent geothermometer precluded an empirical determination of the trapping conditions (pressure and temperature) for the fluid inclusions from the Mavres Petres deposit and Piavitsa prospect. Because of their paragenetic similarities, the carbonate-hosted replacement ore deposits within the Stratoni fault zone are believed to have formed at depths comparable to the Olympias deposit.

The wide range of homogenization temperatures and salinities among type-1 inclusions in each of the study areas (Fig. 11) suggests that they may not all belong to a single fluid inclusion assemblage. Instead, type-1 inclusions may reflect fluid trapping in paragenetically different growth stages of hydrothermal quartz. Alternatively, the range in homogenization temperatures may signify postentrapment reequilibration of some inclusions, although additional petrographic analysis is required to validate this claim. Variations in homogenization temperature and salinity may also be explained by fluid mixing, which is supported by carbon-oxygen isotope data as shown below. Conclusions based on those fluid inclusions defined as type 1, however, are tentative and additional petrographic and microthermometric investigations are required

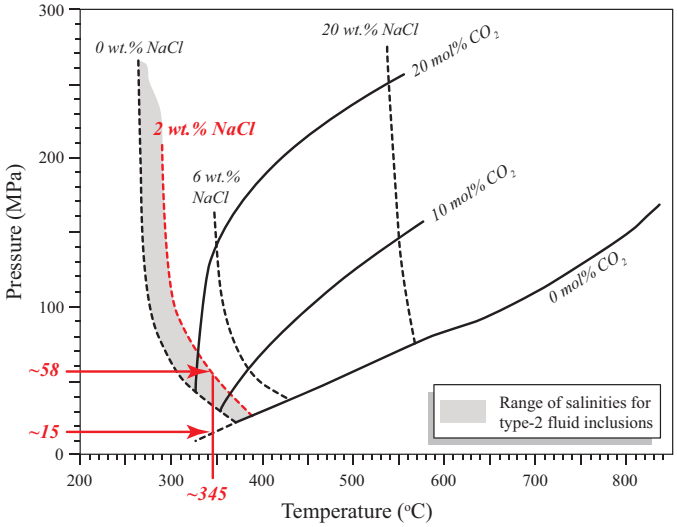

Fig. 10. Pressure-temperature diagram in the system H_2O-CO_2-NaCl, modified after Schmidt and Bodnar (2000), showing the approximate range of trapping pressures (red arrows) at 345°C associated with type-2 fluid inclusions from the Olympias deposit. The maximum trapping pressure is determined from the inferred position of the 2 wt % NaCl solvus, indicated by the solid red line, while the minimum pressure assumes trapping along the H_2O boiling curve.

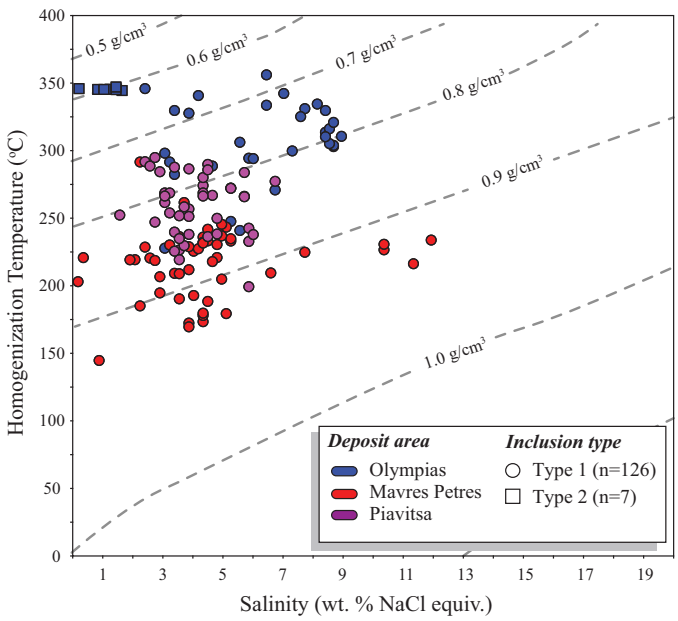

Fig. 11. Microthermometric data from this study are displayed on a salinity versus temperature diagram with density curves representing vapor-saturated H_2O-NaCl solutions plotted for reference (after Wilkinson, 2001).

in order to place tighter constraints on fluid inclusion assemblages and the evolution of the hydrothermal fluids in the district.

Source of hydrothermal fluids and fluid evolution during ore formation

Carbonate $\delta^{13}C$ and $\delta^{18}O$ isotope and quartz fluid inclusion data permit the modeling of isotopic exchange and fluid mixing processes that occurred during hydrothermal alteration and sulfide deposition. Model curves were calculated using published mass balance equations and fractionation factors for calcite (see digital App.) and are constrained by fluid inclusion total homogenization temperatures from this study and previously published data (Gilg, 1993; Kilias et al., 1996). The models assume an initial marble composition of $\delta^{13}C$ = 2‰ and $\delta^{18}O$ = 31‰, consistent with local unaltered marble and published data from Mount Pangeon and Thassos Island to the north of the Kassandra mining district (Varti-Matarangas and Eliopoulos, 2005; Boulvais et al., 2007; Eliopoulos and Kilias, 2011). The model calculations also assume involvement of fluids with magmatic ($\delta^{13}C$ = –7‰, $\delta^{18}O$ = 6‰) and meteoric ($\delta^{13}C$ = –6‰, $\delta^{18}O$ = –5‰) compositions.

Isotopic depletion patterns that characterize the Olympias marble (Fig. 12A) can be interpreted through decarbonation reactions and exchange by means of fluid-rock interaction involving a magmatic fluid at 350°C. The single-stage (batch) decarbonation curve overlaps with a small cluster of the data, but this exchange process does not produce the necessary $\delta^{13}C$ and $\delta^{18}O$ depletion patterns to explain the distribution of the data. The depletion trend on the right-hand side of Figure 12A with the extremely low $\delta^{13}C$ value, however, may be explained by Rayleigh decarbonation at <200°C. Isotopic exchange of carbon between CO_2 in the hydrothermal fluid and crystalline metamorphic graphite contained within the Olympias marbles is not likely given the slow kinetics of diffusion in graphite (e.g., Wada, 1988). Coupled $\delta^{13}C$-$\delta^{18}O$ depletion trends within the Olympias marble are largely attributed to fluid-rock interaction, consistent with the interpretations of Kalogeropoulos et al. (1989). The majority of the data plot between the 0.5 and 0.1X_{CO_2} curves, indicating that isotopic exchange occurred in the presence of a fluid with relatively high dissolved CO_2 contents. Dispersion of the data along the 0.01X_{CO_2} curve, however, could reflect exchange with a carbon-poor fluid, possibly of meteoric origin. Larger $\delta^{13}C$-$\delta^{18}O$ depletion trends correspond to an increase in the water-rock ratio with decreasing CO_2 concentrations (Fig. 12A). This depletion pattern may be explained by isotopic exchange between marble and a magmatic fluid.

Marble sampled from drill core at the Madem Lakkos deposit mostly exhibits high $\delta^{18}O$ values with data scattering between the 0.2 and 0.05X_{CO_2} curves. This indicates that isotopic exchange was influenced by a fluid with relatively low CO_2 concentrations as compared to the Olympias deposit. The depleted $\delta^{13}C$-$\delta^{18}O$ trend exhibited by marbles in the Mavres Petres and Piavitsa areas is also best explained by fluid-rock interaction, likely from a fluid of magmatic composition containing 0.1X_{CO_2} and 0.01X_{CO_2}, respectively (Fig. 12B). A high $\delta^{13}C$ value in a sample of marble from the Piavitsa area may reflect isotopic exchange at lower temperatures (e.g., Ohmoto and Rye, 1979). Increased isotopic depletion of marble from east to west may reflect increasing water-rock ratios with decreasing CO_2 concentration from a factor of ~10 at 0.05X_{CO_2} in the Mavres Petres area to values exceeding 25 at 0.01X_{CO_2} in the Piavitsa area. Two marble samples from the Mavres Petres deposit, highlighted on the left-hand side of Figure 12B, record highly depleted $\delta^{18}O$ values, possibly indicating less magmatic fluid input or a magmatic fluid mixed with a low $\delta^{13}C$ and $\delta^{18}O$ fluid, perhaps derived from meteoric water.

Gangue carbonate minerals associated with sulfide ore at the Olympias deposit show a variable isotopic distribution. Data that plot near the shaded region on Figure 12C likely precipitated from a magmatic fluid with low CO_2 concentration (0.1X_{CO_2}) at temperatures between 350° and 200°C, consistent with fluid inclusion data. Carbonates showing slightly more depleted values may be explained by the involvement of a magmatic fluid at 350°C but with a lower dissolved CO_2 concentration (0.01X_{CO_2}). Gangue carbonates characterized by low $\delta^{18}O$ with no $\delta^{13}C$ modification relative to background marble could have been produced by a carbon-poor fluid at 350°C (Fig. 12C). This pattern, however, requires input of a fluid with a low $\delta^{18}O$ value that was probably meteoric water. The isotopic composition of carbonate minerals associated with skarn and replacement sulfide from the Madem Lakkos and Mavres Petres deposits is similarly explained by the interaction of marble with a magmatic fluid at 450° to 200°C, low dissolved CO_2 concentration (0.01X_{CO_2}), and high water-rock ratios (Fig. 12D). The $\delta^{13}C$ and $\delta^{18}O$ values of carbonate minerals at stylolite contacts overlap with gangue carbonates (Fig. 12D), indicating that the mineralizing fluids not only utilized major strands of the Stratoni fault but also infiltrated marble along pressure solution seams.

Crustiform-textured, quartz-rhodochrosite vein breccias from the Olympias deposit mostly plot within the shaded field defined by a magmatic fluid at 300° to 200°C and low CO_2 concentrations (0.01X_{CO_2}), which similarly describes a minor population of quartz-rhodochrosite vein breccias from the Madem Lakkos, Mavres Petres, and Piavitsa areas (Fig. 12E). The majority of the quartz-rhodochrosite veins from the district are shifted toward highly depleted $\delta^{18}O$ values, which cannot be achieved from a fluid of magmatic composition at temperatures less than 300°C. The distribution of the data, however, can be explained by the mixing of a fluid with low $\delta^{18}O$ value (e.g., meteoric water) at temperatures between 300° and 200°C, consistent with fluid inclusion data.

Source of metals from Pb isotopes

Intrusion-related carbonate replacement deposits commonly show a variety of spatial, geochemical, and isotopic evidence for magmatic-hydrothermal processes and wall-rock reactions. Variations in Pb isotope compositions in many systems reflect a combination of magmatic and wall-rock sources of Pb and, by inference, other metals (Tosdal et al., 1999). Sulfide ores from the Kassandra mining district, however, display a relatively uniform Pb isotope signature, likely from a homogenized deep crustal source. The overlapping relationship of sulfide Pb isotope compositions also suggests that the hydrothermal fluid incorporated Pb from multiple sources, potentially including the Kerdilion and Vertiskos units and associated amphibolites, and the late Oligocene igneous

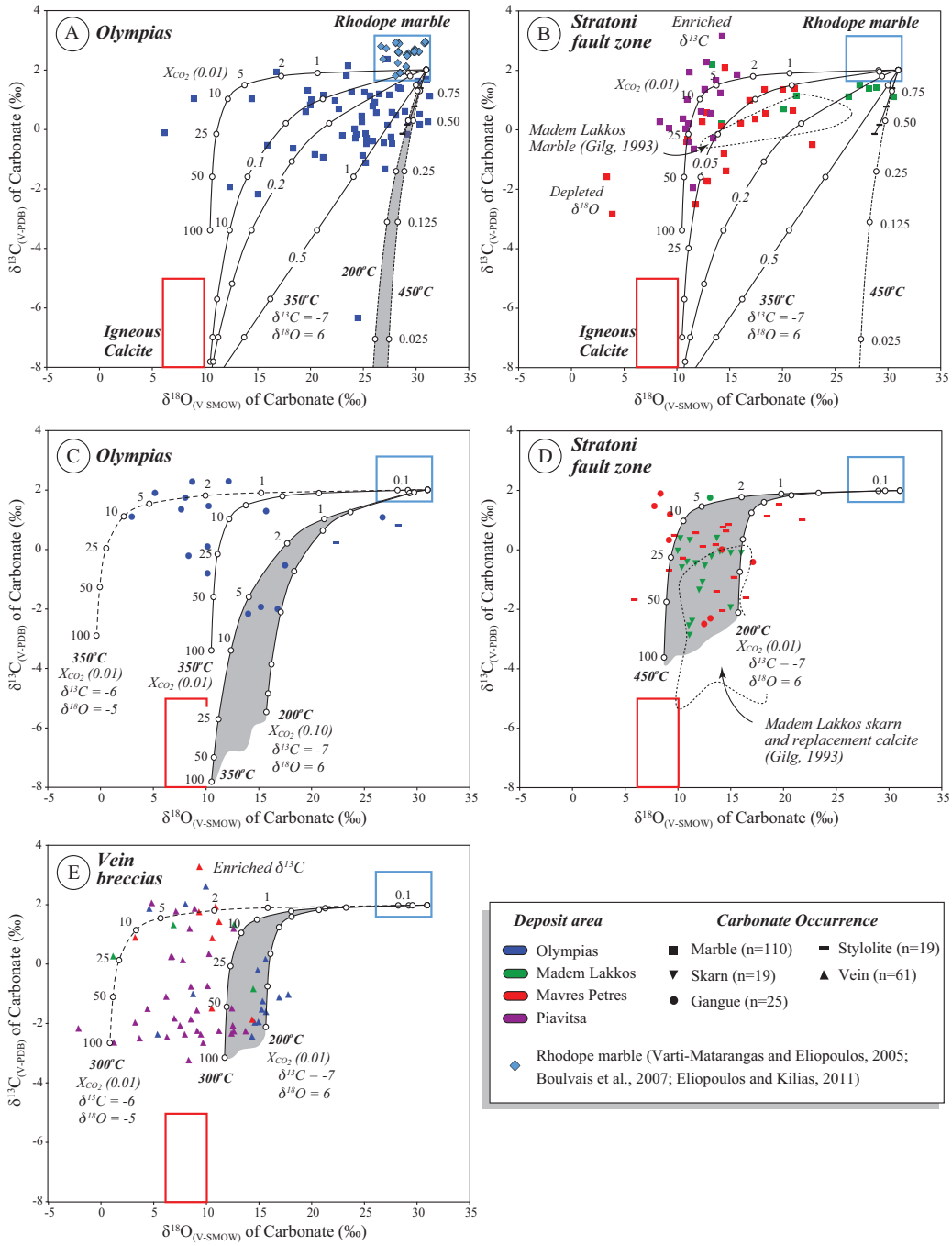

Fig. 12. Plot of $\delta^{13}C_{V\text{-}PDB}$ vs. $\delta^{18}O_{V\text{-}SMOW}$ reported in ‰ for carbonate phases associated with the carbonate replacement deposits from the Kassandra mining district. Note that the carbonate data in this image are displayed with respect to location (color) and style of occurrence (shape). The fields for igneous calcite (Bowman, 1998; Hoefs, 2004) and unaltered Rhodope marble (Varti-Matarangas and Eliopoulos, 2005; Boulvais et al., 2007; Eliopoulos and Kilias, 2011) are illustrated on each diagram along with a series of $\delta^{13}C$-$\delta^{18}O_{calcite}$ evolution curves. Rayleigh and Batch decarbonation curves (displayed on right-hand side of plots A and B) are shown as dotted lines with white circles and as a solid line with black tick marks, respectively. Numbers next to the white circles represent the fraction of carbon remaining in the rock. Fluid-rock interaction curves are shown as solid lines and as dashed lines representing magmatic ($\delta^{13}C$ = –7, $\delta^{18}O$ = +6) and meteoric ($\delta^{13}C$ = –6, $\delta^{18}O$ = –5) fluids, respectively. Numbers next to the white circles indicate the water-rock ratio. Italicized numbers correspond to the proportion of CO_2 in the fluid with temperatures denoted in bold text. Shaded regions represent a range of temperatures that exist for a family of model curves. (A) Marbles from the Olympias deposit. (B) Marbles from the Stratoni fault zone with data from the Madem Lakkos deposit (Gilg, 1993) illustrated by the dotted shape. (C) Gangue carbonate minerals associated with massive sulfide and stylolitic fluid escape structures from the Olympias deposit. (D) Gangue carbonate minerals associated with skarn and massive sulfide, along with stylolitic fluid escape structures from the Madem Lakkos and Mavres Petres deposits. Values reported in Gilg (1993) are illustrated by the dotted shape. E) Quartz-rhodochrosite-calcite veins from the Olympias deposit and deposits within the Stratoni fault zone. Abbreviations: V-PDB = Vienna-Pee Dee Belemnite, V-SMOW = Vienna-Standard Mean Ocean Water.

suite (Fig. 9A-D). Derivation of metals from the early Miocene igneous suite can be ruled out because the carbonate replacement sulfide deposits predate this magmatic event. Previous studies have attempted to fingerprint the causative intrusive source that resulted in skarn and carbonate replacement mineralization within the Stratoni fault zone. Based on Sr and Pb isotope data, Frei (1992) concluded that the Stratoni granodiorite stock did not contribute to the orebodies at the Madem Lakkos deposit. As shown in Figure 9A to D, Pb isotope data are not sufficiently distinct to conclude whether the Stratoni or the Fisoka intrusions contributed to the skarn and replacement sulfide orebodies within the Stratoni fault zone. It is implied by the data that Pb isotopes are inadequate geochemical tracers for identifying metal sources within the Kassandra mining district.

District-scale fluid evolution model for carbonate replacement deposition

The distribution of metals and metal ratio patterns, combined with carbon-oxygen isotope and fluid inclusion data, and the relative structural timing as well as igneous relationships to the sulfide orebodies suggest that the hydrothermal system within the Stratoni fault zone originated from a concealed late Oligocene igneous intrusion in the southeastern sector of the Madem Lakkos deposit (Fig. 13A), although the Stratoni and Fisoka intrusions cannot be ruled out. Similar patterns evident in the Olympias area support a genetic model that involves a hydrothermal fluid that exploited the Kassandra fault zone, which possibly originated from a local late Oligocene igneous intrusion to the east of the Olympias orebody (Fig. 13B).

Carbon-oxygen isotope and fluid inclusion data, together with previously published sulfur isotope data (0.5 ± 1.7‰; Hahn, 2014), indicate that the early skarn and replacement sulfide within the Stratoni fault zone and the replacement orebodies at the Olympias deposit resulted primarily from a fluid of magmatic origin. The carbonate replacement deposits formed in an environment of rapidly fluctuating fluid conditions, probably due to localized fluid-enhanced overpressure conditions with sudden drops in pressure as fault segments episodically dilated during mineralization (e.g., fault-valve mechanism described by Sibson, 2001). This fault-valve process was likely the driving force that permitted the migration of metal-bearing hydrothermal fluids from its source(s), enabling the interaction with receptive host rocks and the subsequent replacement/mineralization of marble horizons confined by faults and preexisting ductile structures.

Fluid inclusion and isotopic data show that cooling of the hydrothermal fluid with an inferred change in fluid pH due to a combination of fluid-rock interaction and fluid mixing were all contributing factors in carbonate replacement mineralization. Carbonate dissolution resulted in neutralization of the hydrothermal fluid, thus inducing the precipitation of metals (e.g., Seward and Barnes, 1997). The degree of carbonate replacement by sulfide was probably a function of the fluid volume that interacted with the hosting lithology, but also increase in the pH of the mineralizing solutions (Bertelli et al., 2009). Low $\delta^{18}O$ values associated with gangue carbonate and low-salinity fluid inclusions trapped in quartz of the younger sulfide phase and the quartz-rhodochrosite vein breccias suggest that the primary magmatic fluid interacted with dilute water of probable meteoric origin during the waning stages of hydrothermal activity.

Comparisons to other carbonate replacement deposits

The polymetallic sulfide orebodies in the Kassandra mining district belong to the intrusion-related class of carbonate-hosted replacement deposit but are distinct when compared to deposits of similar type within the region. The Madem Lakkos, Mavres Petres, and Olympias sulfide ores are characteristically enriched in Au and are hosted by fault-imbricated marble lenses, whereas many replacement-style sulfide deposits in the eastern Mediterranean lack Au in economic quantities (Fig. 14). While similarly hosted by fault-bounded marble, the massive sulfide deposits in the Maden-Thermes district of southern Bulgaria and northeastern Greece, as well as the deposits in the Laviron district of southern Greece, are Au deficient (Kaiser Rohrmeier et al., 2013; Melfos and Voudouris, 2017). Gold is similarly absent in the skarn and replacement sulfide deposits in the Trepča district of Kosovo (Hyseni et al., 2010; Strmić Palinkaš et al., 2013), while gold is present in the Shanac skarn prospect in Serbia (Eldorado Gold Corporation, 2017b). Fault-controlled replacement, skarn, and epithermal veins that comprise the Balya deposit in western Turkey are also enriched in Au (Yigit, 2012) and are geologically similar to the Madem Lakkos deposit. It may be the case, however, that Au was not assayed or reported for some of the deposits in the region. For example, Au was not historically reported for the Madem Lakkos and Mavres Petres deposits, despite their containing significant concentrations.

The sulfide orebodies in the Kassandra mining district exhibit metal distribution patterns that are comparable to many carbonate-hosted replacement sulfide and skarn deposits worldwide, where elevated Cu, generally associated with skarn proximal to an inferred source intrusion, transitions to Zn-Pb with increasing Ag and Mn grades in the peripheral parts of the hydrothermal system. Deposits that show broadly similar zonation patterns occur in the western United States and include the Bingham, Marysvale, Tintic, and Park City districts in Utah; the Eureka and Pioche districts in Nevada; the Leadville and Gilman districts in Colorado; and the Groundhog deposit in the Central mining district of New Mexico (Lindgren and Loughlin, 1919; Morris and Lovering, 1979; Beaty et al., 1986, 1990; Graybeal et al., 1986; Meinert, 1987; Bromfield, 1989; Tooker, 1989; Vikre, 1998). The silver mining districts of Bismark, Santa Eulalia, Naica, and Providencia-Concepcion del Oro in northern Mexico (Prescott, 1916; Megaw et al., 1988; Baker and Lang, 2003) and the Mochito deposit in Honduras (Williams-Jones et al., 2010) also demonstrate metal zonation patterns similar to those of the deposits within the Stratoni fault zone. However, in terms of metal (Ag-Pb-Zn-Cu) concentration and Au endowment, the sulfide orebodies of the Kassandra mining district most closely resemble the deposits within the Eureka (Nevada), Bingham (Utah), and Leadville (Colorado) districts.

Conclusions

The polymetallic sulfide orebodies in the Kassandra mining district belong to the intrusion-related class of carbonate-hosted replacement deposit. These orebodies display geologic

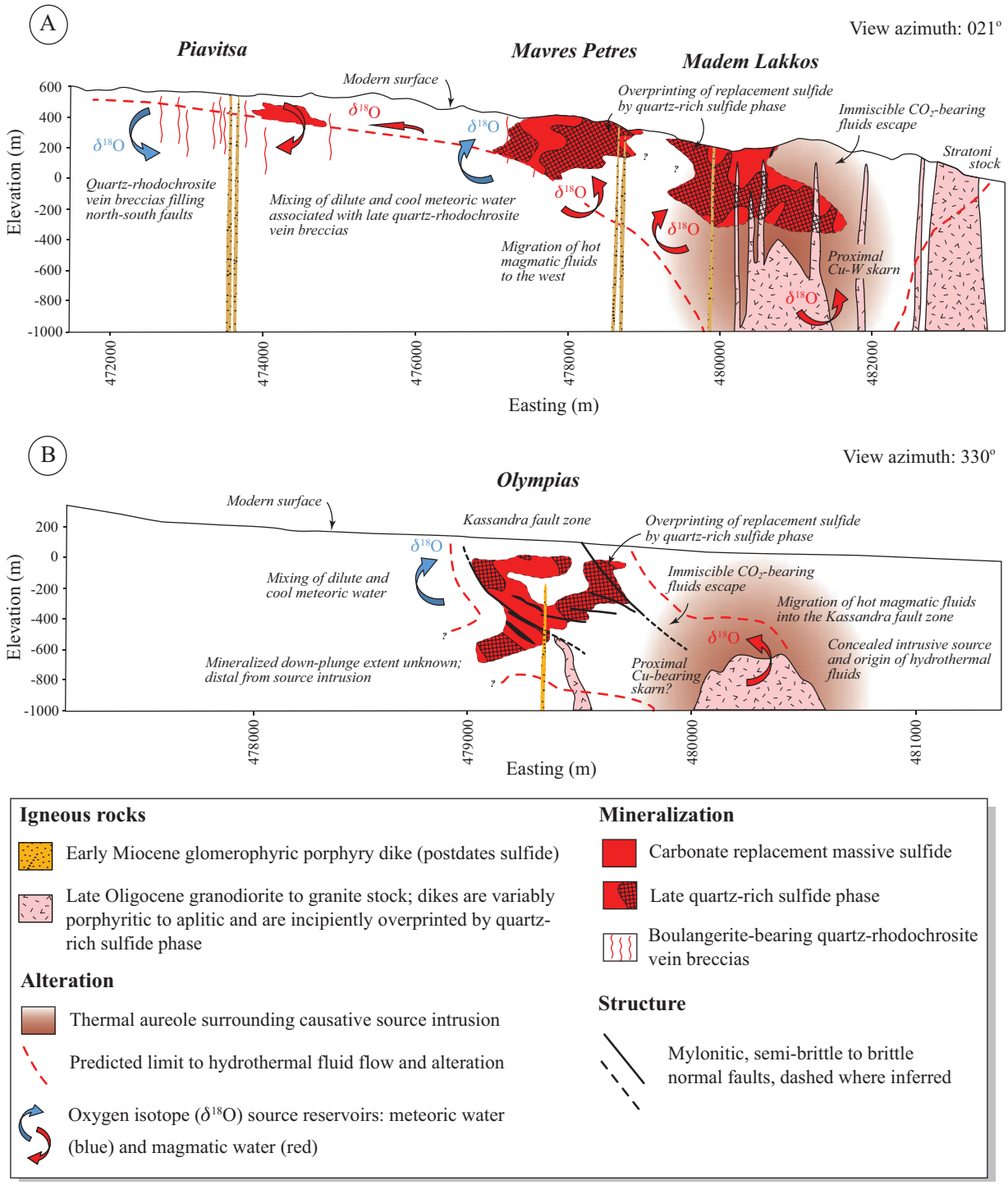

Fig. 13. Genetic model illustrating the evolution of the carbonate replacement deposits within the Kassandra mining district: (A) long-section view of the Madem Lakkos and Mavres Petres deposits and the Piavitsa prospect within the plane of the Stratoni fault zone; (B) cross-section view of the Olympias deposit.

similarities to other deposits of comparable type within the Serbo-Macedonian metallogenic belt and the Aegean region but are distinctive in that they are Au rich. Based on metal grades and Au endowment, the deposits of the Kassandra mining district resemble the carbonate-hosted sulfide orebodies in the southwestern United States.

Marble contained within the Stratoni fault zone hosts the Madem Lakkos and Mavres Petres deposits, where early skarn in the east transitions into carbonate replacement sulfide orebodies to the west. A younger, boulangerite-bearing, quartz-rich sulfide assemblage occurs at each deposit with crosscutting quartz-rhodochrosite vein breccias culminating

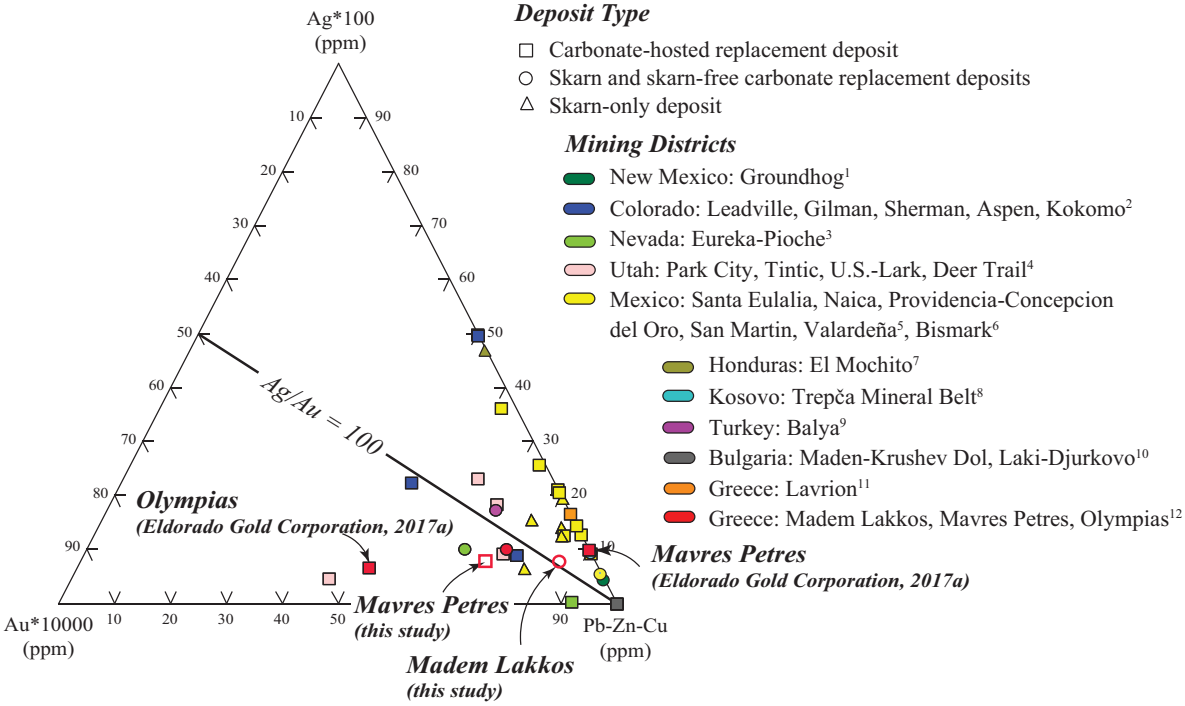

Fig. 14. Ternary diagram of published grades from selected Ag-Pb-Zn ± Cu ± Au carbonate-hosted replacement districts worldwide: (1) Groundhog deposit, Central mining district of New Mexico (Meinert, 1987); (2) Colorado mineral belt (Beaty et al., 1990); (3) Eureka and Pioche districts of Nevada (Shawe and Nolan, 1989; Vikre and Browne, 1999); (4) Park City, Tintic, Bingham (U.S.-Lark), and Marysvale-Deer Trail districts of Utah (Lindgren and Loughlin, 1919; James, 1973; Beaty et al., 1986; Bromfield, 1989); (5) Mexican deposits located in the Santa Eulalia, Naica, Providencia-Concepcion del Oro, San Martin, and Valardeña districts (Megaw et al., 1988) and (6) Bismark district (Baker and Lang, 2003); (7) El Mochito deposit of Honduras (Williams-Jones et al., 2010); (8) Trepča mineral belt of Kosovo (Hyseni et al., 2010); (9) Balya deposit on the Biga peninsula of Turkey (Yigit, 2012); (10) Maden-Krushev Dol and Laki-Djurkovo deposits in the Madan-Thermes district of southern Bulgaria (Kaiser Rohrmeier et al., 2013); (11) Lavrion district in the Attica region of southern Greece (Melfos and Voudouris, 2017); (12) published grades for the Madem Lakkos deposit are after Nebel et al. (1991) and the current measured and indicated resource grades for the Mavres Petres and Olympias deposits are reported in Eldorado Gold Corporation (2017a). The unfilled symbols represent average grades for the Madem Lakkos and Mavres Petres deposits from this study.

late in the mineral paragenesis, which are best developed at the western end of the Stratoni fault zone in the Piavitsa area. The sulfide orebodies at the Olympias deposit are hosted by marbles in contact with, and adjacent to, strands of the Kassandra fault, and are mineralogically and paragenetically similar to the Mavres Petres deposit. Estimated fluid conditions determined from fluid inclusion microthermometric measurements suggest that carbonate replacement mineralization occurred at a paleodepth between 1.5 and 5.9 km, assuming hydrostatic conditions.

Metal distribution patterns within the Stratoni fault zone show elevated Cu in the east, at the Madem Lakkos deposit, with increasing Au concentrations to the west in the Mavres Petres deposit area. Sulfide ore at the Olympias deposit exhibits elevated Cu values in the east with increasing Ag and Ag/Au ratios down-plunge and toward the southeast. Based on previous fluid inclusion studies, the highest temperatures reported in the Stratoni fault zone are associated with skarn and replacement sulfide ore from the Madem Lakkos deposit (Gilg, 1993). Lower temperatures and salinities are characteristic of the younger, quartz-rich sulfide assemblage and quartz-rhodochrosite veins at the Mavres Petres deposit and Piavitsa prospect, respectively. While similarly exhibiting low salinities, the quartz-rich sulfide assemblage at the Olympias deposit formed at temperatures intermediate between those of the Madem Lakkos and Mavres Petres deposits. Fluid inclusions belonging to the system H_2O-CO_2-NaCl at the Madem Lakkos and Olympias deposits are interpreted to represent a trapped immiscible fluid phase coeval with sulfide deposition. A fault-valve mechanism likely resulted in localized and rapid drops in pressure due to slip and dilation along active segments of the Stratoni and Kassandra faults, thus enhancing permeability pathways and allowing the influx of hydrothermal fluids into receptive host rocks. Decreasing temperature and pH changes due to fluid-rock interaction and fluid mixing are considered the probable physiochemical processes that facilitated sulfide deposition.

Carbon and oxygen isotope patterns developed within the Stratoni fault zone indicate that isotopic exchange was principally controlled by fluid–wall-rock interaction, whereas decarbonation and fluid–wall-rock exchange reactions occurred at the Olympias deposit. Gangue carbonate minerals associated with skarn and replacement sulfide from across the district display isotopic compositions intermediate between unaltered marble and igneous values, suggesting the reaction between magmatic hydrothermal fluids and marble. Lower temperatures and salinities characteristic of the boulangerite-bearing, quartz-rich sulfide assemblage and quartz-rhodochrosite vein

breccias, and a low $\delta^{18}O$ value of gangue carbonates are evidence for dilution of a primary magmatic fluid by water of meteoric origin late in the evolution of the hydrothermal system in the Stratoni fault zone and at the Olympias deposit.

The hydrothermal fluids that resulted in the carbonate replacement orebodies within the Stratoni fault zone and at the Olympias deposit were likely derived from late Oligocene igneous activity. Lead isotope compositions of skarn and replacement sulfide overlap with metamorphic basement units and intrusions belonging to the late Oligocene igneous suite, which indicates that sulfide ore likely derived Pb from multiple sources. Based on the Pb isotope data, an inferred causative igneous intrusion responsible for carbonate replacement mineralization in the Stratoni fault zone may be the Fisoka stock; however, this conclusion remains tentative. Structural and igneous relationships to ore, carbon-oxygen stable isotopes, fluid inclusions, and metal distribution patterns are supportive of a zoned, late Oligocene hydrothermal system centered south of the Madem Lakkos deposit and a satellite hydrothermal system centered in the eastern part of the Olympias deposit.

Acknowledgments

The first author acknowledges Eldorado Gold Corporation for kindly providing financial support to perform fieldwork and analytical analyses, including access to their multielement geochemical drill database from the district. Many thanks to everyone in the exploration office at Madem Lakkos for their assistance in the field and logistical support. Discussions on hydrothermal fluid flow with Louis Derry, Larry Cathles, Frank Horowitz (Cornell University), and Kaleb Boucher (Teck Resources) were greatly appreciated. Janet Gabites at the Pacific Center for Isotopic and Geochemical Research at the University of British Columbia is acknowledged for conducting our Pb isotope analyses. Judith Suzuki (Cornell University) and Kate Carroll (University of British Columbia) are thanked for assisting with the carbon-oxygen isotope study, and Malcom Thomas (Cornell University) provided guidance with scanning electron microscopy. This study benefited from the National Science Foundation award number NSF DMR-1719875 to the Cornell Center for Materials Research. Critical reviews by Shaun Barker, David Banks, and Robert Moritz greatly improved the quality of the manuscript.

REFERENCES

Baker, T., and Lang, J.R., 2003, Reconciling fluid inclusion types, fluid processes, and fluid sources in skarns: An example from the Bismark deposit, Mexico: Mineralium Deposita, v. 38, p. 474–495.

Barker, S.L.L., Dipple, G.M., Dong, F., and Baer, D.S., 2011, Use of laser spectroscopy to measure the $^{13}C/^{12}C$ and $^{18}O/^{16}O$ compositions of carbonate minerals: Analytical Chemistry, v. 83, p. 2220–2226.

Barker, S.L.L., Dipple, G.M., Hickey, K.A., Lepore, W.A., and Vaughan, J.R., 2013, Applying stable isotopes to mineral exploration: Teaching an old dog new tricks: Economic Geology, v. 108, p. 1–9.

Baumgartner, L.P., and Valley, J.W., 2001, Stable isotope transport and contact metamorphic fluid flow: Reviews in Mineralogy and Geochemistry, v. 43, p. 365–413.

Beaty, D.W., Cunningham, C.G., Rye, R.O., Steven, T.A., and Gonzales-Urien, E., 1986, Geology and geochemistry of the Deer Trail Pb-Zn-Ag-Au-Cu manto deposits, Marysvale district, west-central Utah: Economic Geology, v. 81, p. 1932–1952.

Beaty, D.W., Landis, G.P., and Thompson, T.B., 1990, Carbonate-hosted sulfide deposits of the central Colorado mineral belt: Introduction, general discussion, and summary: Economic Geology Monograph 7, p. 1–18.

Beinlich, A., Barker, S.L.L., Dipple, G.M., Gupta, M., and Baer, D.S., 2017, Stable isotope ($\delta^{13}C$, $\delta^{18}O$) analysis of sulfide-bearing carbonate samples using laser absorption spectrometry: Economic Geology, v. 112, p. 693–700.

Bertelli, M., Baker, T., Cleverley, J.S., and Ulrich, T., 2009, Geochemical modelling of a Zn-Pb skarn: Constraints from LA-ICP-MS analysis of fluid inclusions: Journal of Geochemical Exploration, v. 102, p. 13–26.

Bodnar, R.J., 1993, Revised equation and table for determining the freezing point depression of H_2O-NaCl solutions: Geochimica et Cosmochimica Acta, v. 57, p. 683–684.

Bottinga, Y., 1968, Calculation of fractionation factors for carbon and oxygen exchange in the system calcite-carbon dioxide-water: Journal of Physical Chemistry, v. 72, p. 800–808.

Boulvais, P., Brun, J.-P., and Sokoutis, D., 2007, Fluid circulation related to post-Messinian extension, Thassos Island, north Aegean: Geofluids, v. 7, p. 159–170.

Bowman, J.R., 1998, Stable-isotope systematics of skarns: Mineralogical Association of Canada Short Course Series, v. 26, p. 99–145.

Bowman, J.R., Willett, S.D., and Cook, S.J., 1994, Oxygen isotope transport and exchange during fluid flow: One dimensional models and applications: American Journal of Science, v. 294, p. 1–55.

Bromfield, C.S., 1989, Gold in the Park City mining district, Utah: U.S. Geological Survey Bulletin 1857-C, p. 14–26.

Brun, J.P., and Sokoutis, D., 2007, Kinematics of the southern Rhodope core complex (north Greece): International Journal of Earth Science, v. 96, p. 1079–1099.

Burg, J.-P., 2012, Rhodope: From Mesozoic convergence to Cenozoic extension. Review of petro-structural data in the geochronological frame: Journal of the Virtual Explorer, electronic edition, v. 42, 44 p.

Cathles, L.M., 1997, Thermal aspects of ore formation, *in* Barnes, H.L., ed., Geochemistry of hydrothermal ore deposits, 3rd edition: New York, John Wiley and Sons, p. 191–227.

Chalkias, S., and Vavelidis, M., 1989, Interpretation of lead-isotope data from Greek Pb-Zn deposits, based on an empirical two-stage model: Geological Society of Greece Bulletin, v. 23/2, p. 177–193.

Coplen, T.B., 1994, Reporting of stable hydrogen, carbon, and oxygen isotopic abundances: Pure and Applied Chemistry, v. 66, p. 273–276.

Cunningham, C.G., Austin, G.W., Naeser, C.W., Rye, R.O., Ballantyne, G.H., Stamm, R.G., and Barker, C.E., 2004, Formation of a paleothermal anomaly and disseminated gold deposits associated with the Bingham Canyon porphyry Cu-Au-Mo system, Utah: Economic Geology, v. 99, p. 789–806.

Darling, R.S., 1991, An extended equation to calculate NaCl contents from final clathrate melting temperatures in H_2O-CO_2-NaCl fluid inclusions: Implications for *P-T* isochore location: Geochimica et Cosmochimica Acta, v. 55, p. 3869–3871.

Dinter, D.A., 1998, Late Cenozoic extension of the Alpine collisional orogen, northeastern Greece: Origin of the north Aegean Basin: Geological Society of America Bulletin, v. 110, p. 1208–1230.

Eldorado Gold Corporation, 2017a, Resources and reserves, www.eldoradogold.com/assets/resources-and-reserves, accessed October 29, 2017.

——2017b, Eldorado Gold provides an update on 2017 exploration programs, www.eldoradogold.com/news-and-media/news-releases/press-release-details/2017/Eldorado-Gold-Provides-an-Update-on-2017-Exploration-Programs/default.aspx, accessed June 26, 2018.

Eliopoulos, D.G., and Kilias, S.K., 2011, Marble-hosted submicroscopic gold mineralization at Asimotrypes area, Mount Pangeon, southern Rhodope core complex, Greece: Economic Geology, v. 106, p. 751–780.

Engel, A.E.J., Clayton, R.N., and Epstein, S., 1958, Variations in isotopic compositions of oxygen and carbon in Leadville limestone (Mississippian, Colorado) and in its hydrothermal and metamorphic phases: Journal of Geology, v. 66, p. 374–393.

Forward, P., Francis, A., and Liddell, N., 2010, Technical report on the Stratoni project Pb-Zn-Ag deposit, northern Greece: European Goldfields Limited, NI 43-101 Report, 54 p.

Frei, R., 1992, Isotope (Pb-Rb-Sr-S-O-C-U-Pb) geochemical investigations of Tertiary intrusions and related mineralizations in the Serbo-Macedonian (Pb-Zn, Sb + Cu-Mo metallogenetic) province in northern Greece: Ph.D. thesis, Zürich, Switzerland, ETH Zürich, 231 p.

——1995, Evolution of mineralizing fluid in the porphyry copper system of the Skouries deposit, northeast Chalkidiki (Greece): Evidence from combined Pb-Sr and stable isotope data: Economic Geology, v. 90, p. 746–762.

Friedman, I., and O'Neil, J.R., 1977, Compilation of stable isotope fractionation factors of geochemical interest: U.S. Geological Survey Professional Paper 440-KK.

Gehrig, M., 1980, Phasengleichgewichte und pVT-daten ternärer mischungen aus wasser, kohlendioxid und natriumchlorid bis 3 kbar und 550°C: Ph.D. thesis, Karlsruhe, Germany, Karlsruhe University, 109 p.

Gilg, H.A., 1993, Geochronology (K-Ar), fluid inclusion, and stable isotope (C, H, O) studies of skarn, porphyry copper, and carbonate-hosted Pb-Zn (Ag, Au) replacement deposits in the Kassandra mining district (eastern Chalkidiki, Greece): Ph.D. thesis, Zürich, Switzerland, ETH Zürich, 153 p.

Gilg, H.A., and Frei, R., 1994, Chronology of magmatism and mineralization in the Kassandra mining area, Greece: The potentials and limitations of dating hydrothermal illites: Geochimica et Cosmochimica Acta, v. 58, p. 2107–2122.

Graybeal, F.T., Smith, D.M., and Vikre, P.G., 1986, The geology of silver deposits, *in* Wolf, K.H., ed., Handbook of stratabound and stratiform ore deposits, v. 14: Amsterdam, Elsevier, p. 1–184.

Hahn, A., 2014, Nature, timing and geodynamic context of polymetallic mineralisation in the Kassandra mining district, north Greece: Ph.D. thesis, London, United Kingdom, Kingston University, 351 p.

Hahn, A., Naden, J., Treloar, P.J., Kilias, S.P., Rankin, A.H., and Forward, P., 2012, A new timeframe for the mineralization in the Kassandra mine district, N Greece: Deposit formation during metamorphic core complex exhumation: European Mineralogical Conference, Frankfurt/Main, Germany, September 2–6, 2012, Proceedings, v. 1, 1EMC2012-742.

Haines, H.S., 1998, A structural synthesis for sector Vb of the Madem Lakkos polymetallic sulfide deposit—northeast Greece: M.Sc. thesis, London, United Kingdom, University of London, 81 p.

Hemley, J.J., and Hunt, J.P., 1992, Hydrothermal ore-forming processes in the light of studies in rock-buffered systems: II. Some general geologic applications: Economic Geology, v. 87, p. 23–43.

Himmerkus, F., Zachariadis, P., Reischmann, T., and Kostopoulos, D.K., 2005, The mafic complexes of the Athos-Volvi-zone—a suture zone between the Serbo-Macedonian massif and the Rhodope massif?: Geophysical Research Abstracts, v. 7, p. 10, 240.

Hitzman, M.W., 1999, Routine staining of drill core to determine carbonate mineralogy and distinguish carbonate alteration textures: Mineralium Deposita, v. 34, p. 794–798.

Hoefs, J., 2004, Stable isotope geochemistry: Berlin, Springer Verlag, 244 p.

Hyseni, S., Durmishaj, B., Fetahaj, B., Shala, F., Berisha, A., and Large, D., 2010, Trepça ore belt and Stan Terg mine—geological overview and interpretation, Kosovo (SE Europe): Geologija, v. 53, p. 87–92.

James, A.H., 1973, Lead and zinc resources in Utah: Utah Geological and Mineralogical Survey Special Studies 44, 66 p.

Janković, S., 1997, The Carpatho-Balkanides and adjacent area: A sector of the Tethyan Eurasian metallogenic belt: Mineralium Deposita, v. 32, p. 426–433.

Kaiser Rohrmeier, M., von Quadt, A., Driesner, T., Heinrich, C.A., Handler, R., Ovtcharova, M., Ivanov, Z., Petrov, P., Sarov, S., and Peytcheva, I., 2013, Post-orogenic extension and hydrothermal ore formation: High-precision geochronology of the central Rhodopian metamorphic core complex (Bulgaria-Greece): Economic Geology, v. 108, p. 691–718.

Kalogeropoulos, S.I., and Economou, G.S., 1987, A study of sphalerite from the carbonate-hosted Pb-Zn sulfide deposits of the eastern Chalkidiki peninsula, northern Greece: Canadian Mineralogist, v. 25, p. 639–646.

Kalogeropoulos, S.I., and Kilias, S.P., 1989, Oxygen (^{18}O) and carbon (^{13}C) isotopic changes in carbonate rocks and minerals in relation to the Olympias Pb-Zn (Au, Ag) sulfide mineralization, E. Chalkidiki, N. Greece: Contribution to metallogeny and exploration: Geological Society of Greece Bulletin, v. 23/2, p. 261–269.

Kalogeropoulos, S.I., Kilias, S.P., Bitzios, D.C., Nicolaou, M., and Both, R.A., 1989, Genesis of the Olympias carbonate-hosted Pb-Zn (Au, Ag) sulfide ore deposit, eastern Chalkidiki peninsula, northern Greece: Economic Geology, v. 84, p. 1210–1234.

Kilias, S.P., and Kalogeropoulos, S.I., 1989, Physiochemical conditions of ore formation of the Olympias Pb-Zn (Au, Ag) sulphide deposit, E. Chalkidiki, based on fluid inclusion studies and arsenopyrite geothermometry. Contribution to metallogeny and exploration: Geological Society of Greece Bulletin, v. 23/2, p. 271–282.

Kilias, S.P., and Madsen, J.K., 1994, H_2O-CO_2-NaCl fluid immiscibility in the carbonate-hosted Olympias Pb-Zn (Au, Ag) sulfide deposit, Macedonia, Greece: Bulletin of the Geological Society of Greece, v. 30/1, p. 445–456.

Kilias, S.P., Kalogeropoulos, S.I., and Konnerup-Madsen, J., 1996, Fluid inclusion evidence for the physicochemical conditions of sulfide deposition in the Olympias carbonate-hosted Pb-Zn(Au, Ag) sulfide ore deposit, E. Chalkidiki peninsula, N. Greece: Mineralium Deposita, v. 31, p. 394–406.

Kockel, F., Mollat, H., and Walther, H., 1977, Erläuterungen yur geologischen karte der Chalkidiki und agrenzender Gebiete 1:100,000 (Nord-Griechenland): Hannover, Bundesanstalt für Geowissenschaften und Rohstoffe, p. 1–119.

Kydonakis, K., Gallagher, K., Brun, J.-P., Jolivet, M., Gueydan, F., and Kostopoulos, D., 2014, Upper Cretaceous exhumation of the western Rhodope metamorphic province (Chalkidiki peninsula, northern Greece): Tectonics, v. 33, p. 1113–1132.

Lindgren, W., and Loughlin, G.F., 1919, Geology and ore deposits of the Tintic mining district, Utah: U.S. Geological Survey Professional Paper 107, 282 p.

Mantzos, L.A., 1989, Geology and lithogeochemistry of the Olympias carbonate-hosted Pb-Zn sulfide deposit, Chalkidiki, Greece: Ph.D. thesis, London, United Kingdom, Imperial College, University of London, 404 p.

McFall, K.A., 2016, Critical metals in porphyry copper deposits: Ph.D. thesis, Southampton, United Kingdom, University of Southampton, 239 p.

Megaw, P.K.M., 1990, Geology and geochemistry of the Santa Eulalia mining district, Chihuahua, Mexico: Ph.D. thesis, Tucson, Arizona, University of Arizona, 461 p.

——1998, Carbonate-hosted Pb-Zn-Ag-Cu-Au replacement deposits: An exploration perspective: Mineralogical Association of Canada Short Course Series, v. 26, p. 258–337.

Megaw, P.K.M., Ruiz, J., and Titley, S.R., 1988, High-temperature, carbonate-hosted Ag-Pb-Zn(Cu) deposits of northern Mexico: Economic Geology, v. 83, p. 1856–1885.

Meinert, L.D., 1987, Skarn zonation and fluid evolution in the Groundhog mine, Central mining district, New Mexico: Economic Geology, v. 82, p. 523–545.

Melfos, V., and Voudouris, P., 2017, Cenozoic metallogeny of Greece and potential for precious, critical and rare metals exploration: Ore Geology Reviews, v. 89, p. 1030–1057.

Morris, H.T., and Lovering, T.S., 1979, General geology and mines of the East Tintic mining district, Utah and Juab counties, Utah: U.S. Geological Survey Professional Paper 1024, 203 p.

Nabelek, P.I., 1987, General equations for modeling fluid/rock interaction using trace elements and isotopes: Geochimica et Cosmochimica Acta, v. 51, p. 1765–1769.

Nebel, M.L., 1989, Metamorphism and polygenesis of the Madem Lakkos polymetallic sulfide deposit, Chalkidiki, Greece: Ph.D. thesis, Golden, Colorado, Colorado School of Mines, 215 p.

Nebel, M.L., Hutchinson, R.W., and Zartman, R.E., 1991, Metamorphism and polygenesis of the Madem Lakkos polymetallic sulfide deposit, Chalkidiki, Greece: Economic Geology., v. 86, p. 81–105.

Neubauer, W.H., 1957, Geologie der blei-zink reichen kieslagerstätten von Kassandra (Chalkidike, Griechenland): Berg- und Hüttenmännische Monatshefte, v. 102, p. 1–16.

Nicolaou, M.N., 1960, L'intrusion granitique dans la région de Stratoni-Olympiade et sa relation avec la métallogenèse: Annales Géologiques des Pays Helléniques, v. 11, p. 214–265.

——1964, The mineralogy and micrography of the sulphide ores of Kassandra mines, Greece: Annales Géologiques des Pays Helléniques, v. 16, p. 111–139.

Nicolaou, M., and Kokonis, I., 1980, Geology and development of the Olympias mine, eastern Chalkidiki, Macedonia, Greece, *in* Jones, M.J., ed., Complex sulfide ores: London, London Institute of Mining and Metallurgy, p. 260–270.

Ohmoto, H., and Rye, R.O., 1979, Isotopes of sulfur and carbon, *in* Barnes, H.L., ed., Geochemistry of hydrothermal ore deposits, 2nd edition: New York, John Wiley and Sons, p. 509–567.

O'Neil, J.R., Clayton, R.N., and Mayeda, T.K., 1969, Oxygen isotope fractionation of divalent metal carbonates: Journal of Chemical Physics, v. 51, p. 5547–5558.

Prescott, B., 1916, The main mineral zone of the Santa Eulalia district, Chihuahua: Transactions of the American Institute of Mining Engineers, v. 51, p. 57–99.

Roddick, J.C., 1987, Generalized numerical error analysis with applications to geochronology and thermodynamics: Geochimica et Cosmochimica Acta, v. 51, p. 2129–2135.

Roedder, E., 1979, Fluid inclusions as samples of ore fluids, *in* Barnes, H.L., ed., Geochemistry of hydrothermal ore deposits, 2nd edition: New York, John Wiley and Sons, p. 657–697.

——1984, Fluid inclusions: Reviews in Mineralogy, v. 12, 644 p.

Ross, K., and Rhys, D., 2013, Petrographic study of a suite of samples from the Olympias deposit, Chalkidiki, Greece: Eldorado Gold Corporation, Unpublished Company Report, p. 217.
Rumble, D., 1982, Stable isotope fractionation during metamorphic devolatilization reactions, *in* Ferry, J.M., ed., Characterization of metamorphism through mineral equilibria: Washington, D.C., Mineralogical Society of America, p. 327–353.
Sagui, C.L., 1928, The ancient mining works of Cassandra, Greece: Economic Geology, v. 23, p. 671–680.
Schmidt, C., and Bodnar, R.J., 2000, Synthetic fluid inclusions: XVI. PVTX properties in the system H_2O-NaCl-CO_2 at elevated temperatures, pressures, and salinities: Geochimica Cosmochimica Acta, v. 64, p. 3853–3869.
Serafimovski, T., 2000, The Lece-Chalkidiki metallogenic zone: Geotectonic setting and metallogenic features: Geologija, v. 42, p. 159–164.
Seward, T.M., and Barnes, H.L., 1997, Metal transport by hydrothermal ore solutions, *in* Barnes, H.L., ed., Geochemistry of hydrothermal ore deposits, 3rd edition: New York, John Wiley and Sons, p. 435–486.
Shawe, D.R., and Nolan, T.B., 1989, Gold in the Eureka mining district, Nevada: U.S. Geological Survey Bulletin 1857-C, p. 27–37.
Sibson, R.H., 2001, Seismogenic framework for hydrothermal transport and ore deposition: Reviews in Economic Geology, v. 14, p. 25–50.
Siron, C.R., Thompson, J.F.H., Baker, T., Friedman, R., Tsitsanis, P., Russell, S., Randall, S., and Mortensen, J., 2016, Magmatic and metallogenic framework of Au-Cu porphyry and polymetallic carbonate-hosted replacement deposits of the Kassandra mining district, northern Greece: Society of Economic Geologists, Special Publication 19, p. 29–55.
Siron, C.R., Rhys, D., Thompson, J.F.H., Baker, T., Veligrakis, T., Camacho, A., and Dalampiras, L., 2018, Structural controls on porphyry Au-Cu and Au-rich polymetallic carbonate-hosted replacement deposits of the Kassandra mining district, northern Greece: Economic Geology, v. 113, p. 309–345.
Stacey, J.S., and Kramers, J.D., 1975, Approximation of terrestrial lead isotope evolution by a two-stage model: Earth and Planetary Science Letters, v. 26, p. 207–221.
Steele-MacInnis, M., 2018, Fluid inclusions in the system H_2O-NaCl-CO_2: An algorithm to determine composition, density and isochore: Chemical Geology, v. 498, p. 31–44.
Strmić Palinkaš, S., Palinkaš, L.A., Renac, C., Spangenberg, J.E., Lüders, V., Molnar, F., and Maliqi, G., 2013, Metallogenic model of the Trepča Pb-Zn-Ag skarn deposit, Kosovo: Evidence from fluid inclusions, rare earth elements, and stable isotope data: Economic Geology, v. 108, p. 135–162.
Taylor, H.P., 1971, Oxygen isotope evidence for large-scale interaction between meteoric ground waters and Tertiary granodiorite intrusions, western Cascades Range, Oregon: Journal of Geophysical Research, v. 76, p. 7855–7874.
——1974, The application of oxygen and hydrogen isotope studies to problems of hydrothermal alteration and ore deposition: Economic Geology, v. 69, p. 843–883.
——1979, Oxygen and hydrogen isotope relationships in hydrothermal mineral deposits, *in* Barnes, H.L., ed., Geochemistry of hydrothermal ore deposits, 2nd edition: New York, John Wiley and Sons, p. 236–277.
Thirlwall, M.F., 2000, Inter-laboratory and other errors in Pb isotope analyses investigated using a ^{207}Pb-^{204}Pb double spike: Chemical Geology, v. 163, p. 299–322.
Thompson, T.B., and Arehart, G.B., 1990, Geology and the origin of ore deposits in the Leadville district, Colorado: Part I. Geologic studies of orebodies and wall rocks: Economic Geology Monograph 7, p. 130–155.
Tödheide, K., and Franck, E.U., 1963, Das zweiphasengebiet und die kritische kurve im system kohlendioxid-wasser bis zu drucken von 3500 bar: Zeitschrift für Physikalische Chemie, v. 37, p. 387–401.
Tooker, E.W., 1989, Gold in the Bingham district, Utah: U.S. Geological Survey Bulletin 1857-E, p. 1–16.
Tosdal, R.M., Wooden, J.L., and Bouse, R.M., 1999, Pb isotopes, ore deposits, and metallogenic terranes: Reviews in Economic Geology, v. 12, p. 1–28.
Valley, J.W., 1986, Stable isotope geochemistry of metamorphic rocks: Reviews in Mineralogy and Geochemistry, v. 16, p. 445–489.
Varti-Matarangas, M., and Eliopoulos, D.G., 2005, Petrographic and stable isotope (C, O) studies of the Pangeon Mountain marbles, northern Greece: Implications for metallogenesis, *in* Mao, J., and Bierlein, F.P., eds., Mineral deposit research: Meeting the global challenge, v. 2: Berlin, Freiberg, Springer-Verlag, p. 931–934.
Vikre, P.G., 1998, Intrusion-related polymetallic carbonate replacement deposits in the Eureka district, Eureka County, Nevada: Nevada Bureau of Mines and Geology Bulletin 110, 52 p.
Vikre, P.G., and Browne, Q.J., 1999, Isotopic characteristics of metal deposits, intrusions, and source rocks in the Pioche district, Lincoln County, Nevada: Economic Geology, v. 94, p. 387–404.
Wada, H., 1988, Microscale isotopic zoning in calcite and graphite crystals in marble: Nature, v. 331, p. 61–63.
Wilkinson, J.J., 2001, Fluid inclusions in hydrothermal ore deposits: Lithos, v. 55, p. 229–272.
Williams-Jones, A.E., Samson, I.M., Ault, K.M., Gagnon, J.E., and Fryer, B.J., 2010, The genesis of distal zinc skarns: Evidence from the Mochito deposit, Honduras: Economic Geology, v. 105, p. 1411–1440.
Yigit, O., 2012, A prospective sector in the Tethyan metallogenic belt: Geology and geochronology of mineral deposits in the Biga peninsula, NW Turkey: Ore Geology Reviews, v. 46, p. 118–148.

Chris R. Siron is an economic and structural geologist with 12 years of research and exploration experience focused on the Cordillera of North and South America and the Tethyan metallogenic belt of southeastern Europe. He has evaluated these regions for porphyry Cu-Mo-Au, polymetallic vein and carbonate-hosted sulfide deposits, orogenic and shear zone-hosted Au systems, and sediment-hosted roll-front uranium deposits. Chris is experienced at defining the metallogenic framework of regions and the structural controls on ore formation through detailed geologic mapping and drill core evaluation, in combination with multielement geochemistry, spectral, and stable isotope analyses. He holds degrees in geological engineering (B.Sc.) and economic geology (M.Sc.) from the Colorado School of Mines, Golden, Colorado, and a Ph.D. in economic geology from Cornell University, Ithaca, New York.